CONTROLLING ADHESION AND ELASTICITY OF MUSSEL FOOT PROTEIN-1 FILMS VIA DOPA-DOPA CROSSLINKING

A Thesis

Presented to the Faculty of the Graduate School

of Cornell University

in Partial Fulfillment of the Requirements for the Degree of

Master of Science

by

Rebecca Michelle Schur

January 2013

ABSTRACT

Adhesive proteins from marine mussels have long been studied for their potential biomedical applications. Mussels form strong, nonspecific, and permanent attachments to surfaces which allow them to maintain a sessile lifestyle in the ocean. Mussel foot protein-1 (mfp-1) forms the protective outer layer that coats the mussel's adhesive construct. It engages in both metal-coordination and covalent intermolecular crosslinks via 3,4-dihydroxyphenylalanine (DOPA) residues- the same side chains which are responsible for this protein's adhesion. In this study, the atomic force microscope (AFM) was used to investigate the effects of lowered DOPA availability due to crosslink formation on the adhesion of mfp-1 to a spherical silica particle.

The natural crosslinking of mfp-1 was mimicked *in vitro* by adding Fe^{3+}, a cation which forms octahedral complexes between three DOPA groups, or $NaIO_4$, an oxidant which induces the formation of covalent diDOPA linkages. Before crosslinkers were added, mfp-1 demonstrated highest adhesion, an ability to spontaneously bridge an opposing surface, and long-range adhesion by extensible mfp-1 chains. Although crosslinks had not been actively generated, the presence of multi-molecular mfp-1 associations was apparent. With the addition of Fe^{3+} and $NaIO_4$, cohesion and elastic modulus of the protein films were higher, and adhesion was lower than in buffer. Neither crosslink allowed for spontaneous bridging. Only metal crosslinks allowed adhesion to be maintained over a long range. A direct correlation was evident between the availability of non-crosslinked DOPA residues and adhesion of the mfp-1 films.

BIOGRAPHICAL SKETCH

Rebecca completed her undergraduate studies in the Materials Science and Engineering department at Cornell University in May 2010. She began researching marine mussel adhesion in Dr. Delphine Gourdon's laboratory in the fall of 2009 for her senior thesis. She then remained at Cornell to pursue an M.S. as she continued to work in this field. After completing her master's degree, Rebecca will enter the Ph.D. program in Biomedical Engineering at Case Western Reserve University.

ACKNOWLEDGEMENTS

I would like to thank my advisor, Dr. Delphine Gourdon, for her guidance and support throughout the time I have worked in her laboratory. The members of the Gourdon research group, Roberto Andresen, Karin Wang, and Fei Wu, were always eager to discuss my research and challenge my thinking. Heather Schopper assisted as an undergraduate researcher throughout this project. Dr. Kit Umbach and Teresa Porri were ever patient in assisting with the technical operation of the AFM. I would also like to thank Dr. Herbert Waite and Dr. Dong-Soo Hwang (Marine Sciences Institute, University of California, Santa Barbara) for providing the purified mfp-1 samples used in these experiments, and for valuable discussions of the results.

This work was partially funded by NSF-ENG CMMI (Grant Award #1031068), a Seed Grant from the Cornell Center for Materials Research through NSF-DMR MRSEC (Grant Award #0520404), and Cornell Engineering Learning Initiatives (ELI) support for undergraduate research. This work made use of STC shared experimental facilities supported by the National Science Foundation under Agreement #ECS-9876771.

TABLE OF CONTENTS

LIST OF TABLES

LIST OF FIGURES

CHAPTER 1

INTRODUCTION

Strong adhesives are an integral component of many engineering designs. Commercial glues are available which can bind a wide variety of surfaces, regardless of their chemistry and roughness. Effective function of these materials, however, is typically limited to their use in air, as fundamental physicochemical properties of water weaken the intermolecular forces which create adhesive interfaces.

One challenge toward wet adhesion is the high dielectric constant of water. Charge-charge interactions follow Coulomb's law, which states that the electrostatic force F between two charged entities, Q_1 and Q_2, is inversely proportional to its dielectric constant ϵ [54]:

$$F = \frac{Q_1 Q_2}{\epsilon r^2} \tag{1.1}$$

The polarity of water molecules increases the dielectric constant of deionized water to approximately 80, relative to 1 in vacuum and only slightly higher than 1 in air. With the addition of ions, the dielectric constants of aqueous solutions are further increased due to the effects of Debye screening. Weakening of charge-charge interactions has strong implications for wet adhesion, because all non-covalent bonds, such as dipole-dipole interactions, hydrogen bonds, and van der Waals forces, result from attractions between opposite charges, both permanent and transient. These intermolecular forces are precisely the interactions which dominate adhesive interfaces. In high dielectric media such as water or aqueous solutions, adhesive bonds are inherently weaker than the same

system in air.

In addition to weakening electrostatic forces, water molecules have a propensity to form a weak boundary layer near surfaces [32]. Between hydrophilic solids, this film is difficult to remove, and it creates a positive disjoining pressure which repels the surfaces from one another. An effective adhesive must have the capacity to displace this layer of water molecules. If it is unable to do so, its adhesive strength in a wet environment is limited by its interaction with the water molecules, rather than its ability to bridge with the opposing surface. Additionally, adhesion of synthetic polymers in water is further weakened by the degradation of adhesives due to hydrolysis and swelling [76]. The difficulties of forming strong bonds to surfaces while maintaining the structural integrity of the interface causes most commercial adhesives to fail when applied in water.

Markets for improved biomedical adhesives exist in many human health-related fields, ranging from dentistry, to surgery, to wound healing. Materials for these applications must function in the aqueous environment of the human body, and overcome the challenges described above. Biomedical adhesives must fulfill an additional requirement: any substance that will be introduced into the body must be biocompatible. Two types of surgical glues, fibrin sealants and cyanoacrylates, are currently available [61]. Each of these materials possesses distinct advantages and disadvantages for these applications. Fibrin, a class of sealant, imitates the body's natural wound healing pathways by acting as a coagulant. It works in conjunction with the immune system to induce the formation of clots which isolate the exposed wound, contain fluids, and promote tissue repair. Some components of fibrin cannot be produced syntheti-

cally and must be obtained either autologously, which requires that the patient be relatively healthy, or from a donor, which increases the risk of infection and rejection.

In contrast, cyanoacrylates are entirely synthetic. They rapidly cure, form strong adhesive bonds, and do not readily degrade in water. The brittle nature of cyanoacrylates has made them poorly suited for large wounds and dynamic moving parts of the body. Furthermore, their cytotoxicity and carcinogenicity present risks for biomedical use. Other synthetic adhesives which have been developed suffer from poor biocompatibility as well as low adhesive strengths.

Rather than addressing biomedical adhesives from a synthetic perspective, this work will take a biomimetic approach by studying a natural system of wet adhesion. Many marine organisms, such as the blue mussel *Mytilus edulis*, have evolved mechanisms which allow them to adhere to surfaces in the ocean. Mussels inhabit rocky intertidal zones [68], where they must regularly withstand waves with water velocities approaching 10m/s, and accelerations up to 400m/s^2 [11]. Combining hierarchical geometries with a unique assembly of proteins, marine mussels are able to permanently adhere to nearly any surface available, natural or man-made, regardless of the chemistry of the substrate. This versatility enables the species to survive without being displaced by currents, tides, or turbulent storms. The proteins responsible for mussel adhesion have been shown to bind soft tissues with similar strengths to fibrin sealants [55], promote cell adhesion, and are non-cytotoxic [20]. With more research, mussel adhesion holds promising implications for the development of innovative underwater adhesives and their applications as biomedical glues.

CHAPTER 2

FUNDAMENTALS OF ADHESION

Adhesion between two opposing surfaces can occur through a variety of mechanisms. For example, adhesion can be mechanical, where physical interlocking between surfaces holds them together. This is the mechanism which enables strong attachments in velcro. Adhesion can be due to dispersion forces, where the sum of many van der Waals interactions between surfaces allow them to adhere to one another. The type of adhesion at the focus of this work is chemical adhesion in which a chemical bonds form between the atoms at the surfaces. These can be covalent, ionic, or hydrogen bonds.

2.1 Work of Adhesion

The work of adhesion, W_{AB}, is defined as the energy required to separate two flat, smooth surfaces from full contact to infinite separation (Figure 2.1) [38].

The work of adhesion is related to the surface energies γ_i of each solid and the energy of interface γ_{AB} by the Young-Dupré equation:

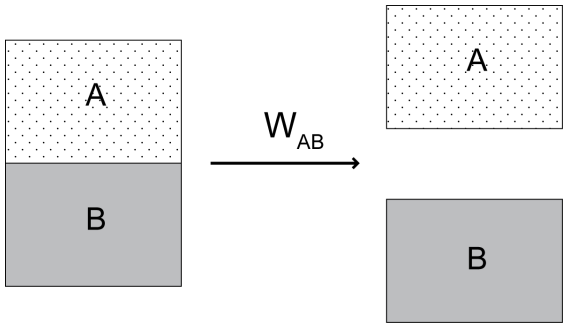

Figure 2.1: Work of adhesion, W_{AB}, is a measure of the energy to separate surfaces from contact.

$$W_{AB} = \gamma_A + \gamma_B - \gamma_{AB} \tag{2.1}$$

2.2 Derjaguin Approximation

The work of adhesion is a materials-specific property and independent of the geometry of contact. For a more experimentally relevant analysis of surface interactions, however, it is necessary to account for this. For contact between two spheres, with radii R_1 and R_2, the Derjaguin approximation relates the normal force *F(D)* to the work of adhesion *W(D)* through the following relation [12]:

$$F(D)_{spheres} = -\frac{\partial W(D)_{planes}}{\partial D} = 2\pi R_{eff} W(D) \tag{2.2}$$

where $R_{eff} = \frac{R_1 R_2}{R_1 + R_2}$.

The sphere-on-flat geometry employed in the AFM experiments in this work is considered a limiting case of two spheres, in which the radius of the flat sample surface is treated as $R_2 >> R_1$. In this case, the effective radius $R_{eff} = R_1$.

2.3 Contact Mechanics

Contact mechanics theories describe the interactions of solid surfaces at interfaces. When a compressive normal force F_n is applied, the solids press into one another to an indentation depth δ, and flatten with a corresponding change in contact radius a. These quantities, which can be measured experimentally, are

related to one another based on the geometry of the contact, the interfacial free energy W, and the stiffness of each surface K [7, 38].

2.3.1 Hertz Theory

The elastic contact between two non-adhering solids is described by the Hertz model of contact mechanics [30], and governed by the following equations:

$$\delta = \frac{a^2}{R} = \frac{F_n^2}{RE^2} \tag{2.3}$$

Since the surfaces in this model do not interact energetically, there is no adhesion force F_{ad} between them. When contact is formed or broken at $\delta=0$, the contact radius is also zero.

2.3.2 Johnson-Kendall-Roberts Theory

While the Hertz model is appropriate for non-adhering solids, soft and biological materials are often adhesive. The Johnson-Kendall-Roberts (JKR) theory accounts for the effects of surface energy on the contact between solids [41]. Here, the adhesion force F_{ad} when the surfaces are separated is related to the interfacial energy according to the following equation:

$$F_{ad(JKR)} = \frac{3}{2}\pi RW \tag{2.4}$$

Unlike in the Hertz theory, in JKR mechanics, both contact area and indenta-

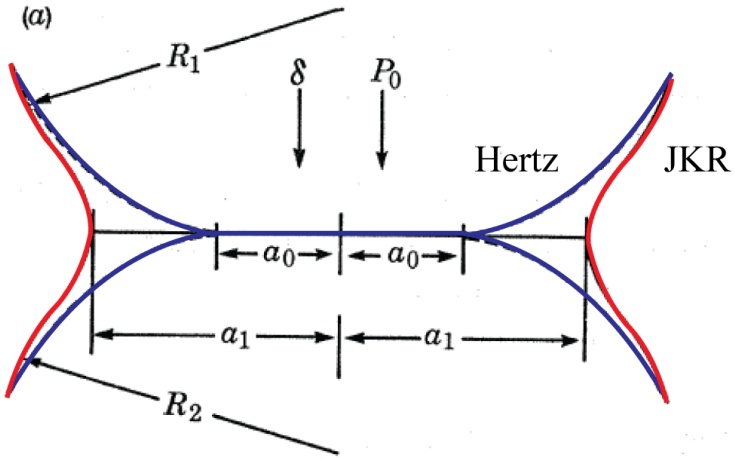

Figure 2.2: Deformation of solids for non-adhesive Hertz (blue) and adhesive JKR (red) models of contact mechanics. Adapted from [41].

tion are positive at zero applied load. These quantities are related to the applied normal load by the following equations, respectively:

$$a^3 = \frac{R}{K}\left[\sqrt{F_{ad}} + \sqrt{F_n + F_{ad}}\right]^2 \tag{2.5}$$

$$\delta = \frac{a^2}{R} - \frac{4}{3}\sqrt{\frac{aF_{ad}}{RK}} \tag{2.6}$$

Zero indentation ($\delta = 0$) occurs at $F_n = -\frac{8}{9}F_{ad}$ [47].

The Hertz (blue) and JKR (red) predictions for elastic contact of a deformable sphere on a rigid, flat surface are summarized schematically in Figure 2.3.2.

In viscoelastic materials, as typical for soft and biological materials, a hysteresis in adhesion energy is often measured between the loading and unloading contact regimes. When this disparity occurs, the adhesion force is lower at the onset of contact than during separation. This occurs because the formation

of interfacial bonds, and by extension the increase in contact area, are time-dependent processes.

2.3.3 Elastic Modulus

Elastic modulus is extracted from the contact mechanics relations from the calculated stiffness values. Assuming that one surface is much more rigid than the other, i.e. $E_1 >> E_2$, the modulus of the more compliant material can be determined using the following equation:

$$E = \frac{3}{4}K(1-\nu^2) \tag{2.7}$$

Where ν is the Poisson's ratio. According to convention, biological materials are considered incompressible, and are assigned ν=0.5.

CHAPTER 3

MUSSEL SYSTEM

Mussels form permanent, nonspecific attachments to available surfaces, regardless of the chemistry of the substrate [9]. This ability gives the organisms the versatility to securely anchor themselves in response to rapid changes in their environment. To accomplish this, mussels generate an extracellular byssus, an assembly of proteins which tether the shell of the animal to its desired surface.

Attachments between the mussel byssus and its substrate consists of four distinct sections (Figure 3):

1) Precollagen fibers which protrude from the shell (brown),

2) Collagen-binding matrix proteins (blue),

3) A structural foam-like plaque (gray),

4) An adhesive footprint (pink), and

5) A protective outer cuticle (red).

A typical mussel lays down 50-100 threads, each of which is approximately 3-4cm in length [77]. The plaque, which is the thickest portion of the attachment, is 1-2mm in diameter. The average mussel takes no more than five minutes to extrude a thread. Once generated, it does not require a resting interval to set before it is employed as a functional load-bearing attachment.

The byssus is generated by the foot muscle which is able to leave the shell and temporarily hold onto a surface [75, 77]. In the phenol gland of the foot, the byssal proteins are synthesized and stored in secretory vesicles within the cells.

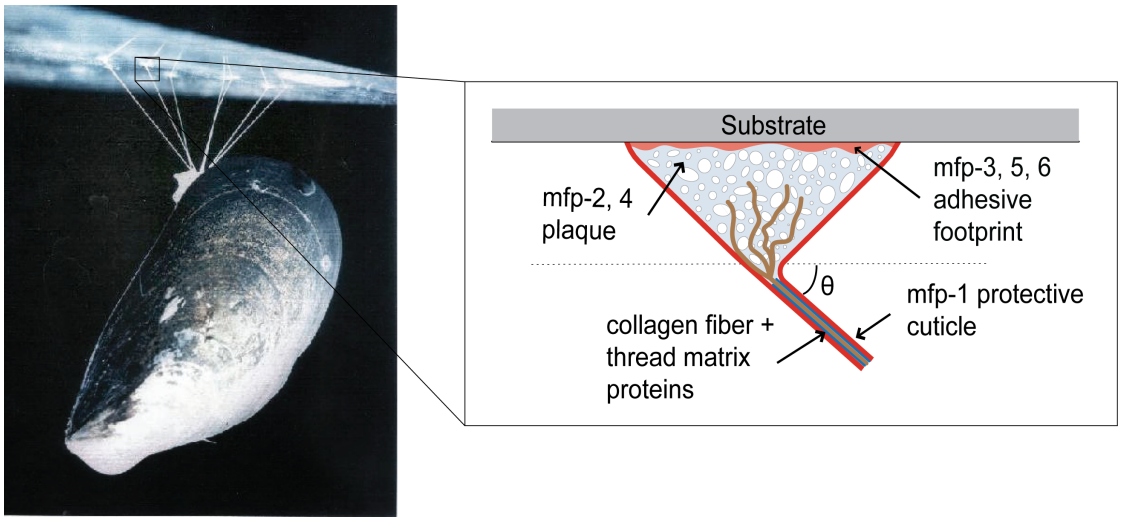

Figure 3.1: (Left) Photograph of a mussel attached to a glass surface using a set of byssal threads. (Right) Organization of proteins in the byssus.

These proteins are released sequentially, beginning with the interfacial proteins and followed by those destined for the plaque, into the distal depression at the far end of the foot. The depression creates a suction against the surface, generating an opening of negative pressure to temporarily hold onto the surface while providing a space into which the byssal proteins can be secreted. The process leading to the formation of the cuticle surrounding the threads has yet to be determined, however, it is believed that it is extruded from the ventral groove after the interface and plaque have been generated.

Precollagen Fibers

Three forms of precollagen are present in the byssal threads: preCOL-D (distal), preCOL-P (proximal), and preCOL-NG (non-graded) [82]. These species are present in a gradient along the length of the thread, with preCOL-D dominant

near the plaque, preCOL-P dominant near the shell, and a uniform distribution of preCOL-NG. Mechanical properties of these preCOLs vary, resulting in a stiffness gradient which is more compliant toward proximal end of the thread. Each preCOL molecule is symmetric and contains three types of domains: a collagen domain, two flanking domains, and two His-rich terminating sequences [8, 82]. The collagen domain contains $(\text{Gly-X-Y})_n$ repeats, in which 20 mol% of X and Y are Pro or Hyp. The flanking domains contain the predominant differences between the three collagen species and are the source of their distinct mechanical properties. In preCOL-D, the flanking domains resemble the primary structure of the stiff silk-fibroin protein, whereas in preCOL-P, the flanking domains are elastin-like, leading to more compliance under uniaxial tension. In preCOL-NG, these domains resemble the glycine-rich cell wall proteins found in plants. Finally, the terminating domains of the byssal preCOLs are rich in His residues. These residues are able to form reversible crosslinks with metal cations such as Zn^{2+}, resulting in a globular conformation of the domain. Under tensile strain, these crosslinks are able to break, allowing the flanking domains to unfold [27]. Upon relief of this tension, these crosslinks can be reformed, and the stiffness of the preCOL fibers is recovered.

Thread Matrix Proteins

In the proximal portion of the byssal thread, the preCOL fibers are largely disordered and loosely packed. The remainder of the thread volume is occupied by non-collageneous thread matrix proteins (TMPs) rich in Gly, Tyr, Asx, and Glx [70]. These proteins are between 40-50kDa, and do not contain DOPA. The primary structure of TMPs are homologous to the collagen-binding A domains of

Protein	Mass (kDa)	Isoelectric point	% DOPA	Location in byssus	Ref.
Mfp-1	110	10	15	Cuticle	[17, 81]
Mfp-2	45	10	3-5	Plaque	[64]
Mfp-3	5-7	8-10	20	Interface	[59]
Mfp-4	80	8.4	2	Plaque	[92]
Mfp-5	9	9.8	27	Interface	[78, 91]
Mfp-6	12	9.3	4	Interface	[91]

Table 3.1: Properties of mussel foot proteins.

von Willebrand Factor, a glycoprotein found in the circulatory system, as well as the integrin $\alpha_I 1$. Small quantities of a distinct TMP have been found in the distal thread [65]. The distal TMP is not homologous with already characterized proteins, however it is prone to deamidation of the Asn residues, a common feature in other collagen-binding proteins.

The preCOL fibers are protected and connected to the surface by a set of proteins unique to the mussel byssus, termed "mussel foot proteins" (mfps). These are alkaline proteins, and contain large amounts of the post-translational modification of Tyr, 3,4-dihydroxyphenyl-L-alanine (DOPA). Similar to the His-coordination of Zn^{2+} found in pre-COL, mfps sequester ions from their surrounding environment to form crosslinks for mechanical stability. Properties of these proteins are summarized in Table 3.

Plaque

Mfp-2 and mfp-4 comprise the plaque which anchors the ends of the preCOL fibers and binds to the footprint. Structurally, the plaque resembles a porous

foam. Mfp-2 is rich in Cys residues, and contains a low concentration of DOPA residues, which are located at the N- and C- termini of the protein [64]. Mfp-2 cohesion depends on crosslinks with metal cations [36]. In the plaque, iron is found to be co-localized with mfp-2, and *in vitro* experiments have shown that this protein is able to form cohesive bridges only in the presence of cations such as Fe^{3+} and Ca^{2+}. Furthermore, mfp-2 binds to the interfacial protein mfp-5, providing a link between the structural plaque and the strong glues at the interface.

Mfp-4 is found at the juncture between the plaque and the preCOL threads [92]. This protein contains His-rich repeating domains concentrated at the N-terminus, and is able to bind with metal ions such as Cu^{2+}. It has been speculated that the metal binding affinity of mfp-4 allows it to anchor the His-rich domains of the preCOL fibers into the plaque.

Adhesive Interface

Mfp-3, mfp-5, and mfp-6 form the interface which bridges the plaque to the surface. Mfp-3 and mfp-5, both of which have high DOPA contents, are considered the main proteins responsible for adhesion, and mfp-6 aids in this function. All three are small proteins, with no significant repetitive sequences of amino acids. Mfp-3 is primarily comprised of Gly, Asp, DOPA, Trp, and Arg [59]. 40-80% of the Arg residues are modified to hydroxyarginines, and numerous hArg-DOPA dipeptides are present throughout the primary sequence.

Mfp-5 contains the highest DOPA content in the byssus. It is primarily composed of Gly, DOPA, Lys, and Ser, of which most of the Ser residues are phos-

phorylated [78]. The presence of phosphoserine may provide an alternate adhesive pathway to bind to mineral and Ca^{2+}-rich surfaces, such as the shells of other mussels.

Mfp-6 is primarily composed of Gly, Tyr, and Cys residues, in which one of five Tyr residues have been post-translationally modified to DOPA [91]. The thiol groups in mfp-6 behave as reducing agents to reverse the natural oxidation of DOPA residues in the remaining interfacial proteins [87]. The thiols may also react with the DOPA residues of mfp-3, increasing cohesion of the adhesive interface.

Cuticle

Coating these byssal components is a protective cuticle, primarily composed of mfp-1. This layer shields the thread and plaque from chemical and physical abrasions, and must accommodate the strain of the underlying extensible collagen fibers. Physical, chemical, and mechanical properties of mfp-1 and its role in the byssus will be discussed in detail in Section 3.1.

Role of DOPA

One unique element of mussel foot proteins is their high incidence of the amino acid DOPA. DOPA is a post-translational modification of tyrosine, containing two hydroxyl groups which functionalize the phenol ring of the side chain (Figure 3). DOPA is a highly unstable molecule, and can easily undergo oxidation if it is not maintained at low pH or in a reducing environment.

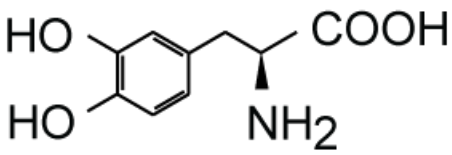

Figure 3.2: Chemical structure of DOPA.

DOPA is believed to be responsible for strong adhesion of mfp's [88, 89], and synthetic mimics of mussel glue have largely relied on this functionality to generate adhesion [46, 21, 44].

The DOPA side chain is able to bond to surfaces using three primary pathways: (1) π-electron overlap with other ring structures, (2) Covalent and coordination bonding between catechol oxygens and surface metal atoms, and (3) Hydrogen bonding via the hydroxyl groups. While π-electron overlap has not been directly demonstrated for this amino acid in isolation, DOPA-containing mfp-1 has been shown to adsorb more strongly to a polystyrene (PS) substrate, which contains benzyl rings, than poly(octadecyl methacrylate), a different hydrophobic surface which lacks ring structures [4, 3]. Because DOPA has no other means by which it can interact with hydrophobic surfaces, it is likely that the catechol ring is able to orient itself parallel to surfaces such as PS and bond through $\pi - \pi$ overlap. Furthermore, when adsorbed onto Au, DOPA aligns parallel to the surface, which likely enables it to form these $\pi - \pi$ bonds [83]

Recently, interest in the use of DOPA as an organic photosensitizer in dye-sensitized solar cells has prompted computational studies of the interaction of DOPA with inorganic oxide surfaces. On TiO_2, hydrogen bonds can be formed between the hydroxyl groups of DOPA and oxygen atoms on the oxide surface [73]. In the oxidized state, oxygen atoms on DOPA are able to covalently bond with the Ti atoms on the surface in a monodentate [73] or a bidentate [62, 74]

configuration, depending on the crystal face to which it binds. In these configurations, the adhesion energy of DOPA to TiO_2 ranges from 25 to 30kcal/mol.

On silica, the surface of interest for the experimental results presented in this work, computational studies using density functional theory and molecular dynamics have investigated the geometry of the catechol at the surface [51], as well as the kinetics of water displacement during binding [52]. In these simulations, the ring was nearly perpendicular to the surface of the silica, which oriented its hydroxyl groups to form four hydrogen bonds with the silanols on the surface (Figure 3). The binding energy for this interaction was 33kcal/mol. With water molecules present, as discussed above, it is instructive to consider the possibility that DOPA could H-bond with the weak boundary layer of water that had adsorbed to the SiO_2 surface. When compared to DOPA-silica bonding, however, interactions with intervening water molecules were much weaker than DOPA directly interacting with the surface. MD simulations confirmed that the catechol group is able to displace water molecules from the hydrophilic silica surface, and form H-bonds with the silanol groups.

Experimentally, the binding energy of DOPA to TiO_2 has been measured by tethering single DOPA molecules to atomic force microscope (AFM) tips and measuring the adhesion forces [45]. Adhesive bonds were ruptured with forces ranging from 400-1200pN, and a binding energy of 22.2kcal/mol was calculated.

SFA experiments have been performed for DOPA-containing polymers on mica, a substrate commonly used for investigations of adsorbed biomacromolecules. Mica is an aluminosilicate crystal which is easily cleaved on a macroscopic scale along its (001) planes, exposing the K^+ ions which maintain the elec-

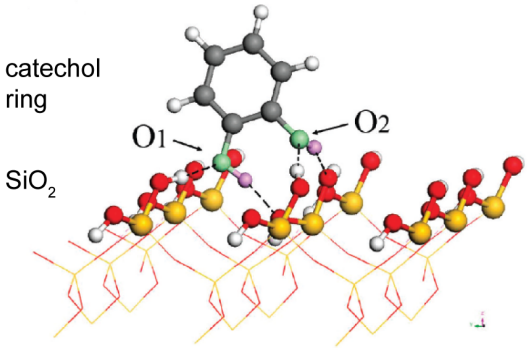

Figure 3.3: Adsorption of catechol on SiO_2. Four hydrogen bonds form between the hydroxyl groups and the silanols on the surface. Yellow atoms represent Si, red and green atoms represent O, gray atoms represent C, and white atoms represent H. Dashed lines represent H-bonding between the catechol and the surface. Adapted from [51].

trical neutrality of the material [19]. The interaction strength between DOPA and mica is weaker than on TiO_2 or SiO_2, with a lower limit of 0.04kcal/mol [2]. The mechanism of DOPA-mica bonding is likely different than for the oxide surfaces discussed above, as the silicon atoms are spaced too far apart (0.52nm) for DOPA to adopt a bidentate configuration. In the basal plane, however, O atoms are spaced 0.30nm apart, which is near the 0.29nm spacing between hydroxyls in DOPA. As a result, it has been speculated that this lattice matching may enable DOPA to form two hydrogen bonds with the oxygen atoms on mica's surface.

3.1 Mussel Foot Protein-1

Mfp-1 is the primary component of the protective cuticle surrounding the byssal threads. Previous work has shown that the superficial adhesive properties of

this protein and the cohesion of the mfp-1 - mfp-1 interaction, can be modulated with mechanical [48] and chemical [90] stimuli. Its versatile functionality has made mfp-1 an attractive candidate for commercial applications.

3.1.1 Structure

Primary Structure

Mfp-1 is the largest of the non-collageneous byssal proteins, with a molecular weight of 108 kDa. It is an alkaline protein, with an isoelectric point of 10. Its primary structure consists of ten- and six- amino acid repeats, referred to as the decapeptide and hexapeptide. The amino acids in the decapeptide repeat are as follows: AKPSY***P*****P**T***Y***K, in which ***P*****,** **P**, and ***Y*** are the post-translational modifications 4-hydroxyproline, 3,4-dihydroxyproline, and DOPA, respectively [17, 81] (Figure 3.1.1). The hexapeptide sequence contains the first and the final three residues of the decapeptide: AKPT***Y***K. A full mfp-1 molecule contains 72 decapeptides and 14 hexapeptides, with the six-residue variants distributed throughout the molecule [17]. At the N-terminus is a non-repetitive domain primarily composed of hydrophilic residues.

Secondary Structure

Typically, proteins with such repetition in their primary structure fold into a stable, native conformation, such as the α-helix in the winter flounder's antifreeze protein [66] or the β-sheet in silk fibroin [18]. The lack of hydrophobic residues throughout mfp-1, however, removes the principle driving force for

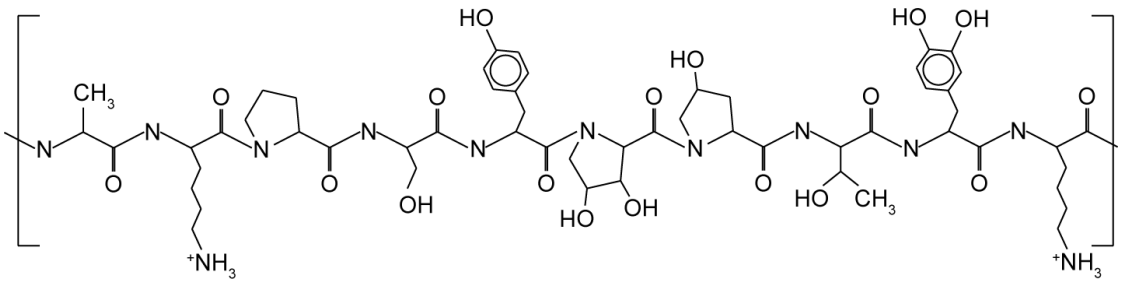

Figure 3.4: Primary structure of the mfp-1 decapeptide repeat.

protein folding [13]. Experimental characterizations of the conformation of mfp-1 and its constituent decapeptide have confirmed this lack of structure. Circular dichroism has suggested a 65-75% random structure for mfp-1. This value was not significantly altered by the addition of harsh chemical denaturants, which typically unfold proteins by destabilizing hydrogen bonding; surfactants, which destabilize the hydrophobic cores of proteins; or increased temperature [85].

Using NMR, secondary structural information has been derived for recombinant mfp-1 decapeptides, and the resulting structures are atypical for folded proteins. In good solvent, the decapeptide forms a helix similar to a bent [58] or polyproline type-II helix [42] (Figure 3.1.1). The decapeptide does not precisely follow either of these standard forms, as its helix is not stabilized by hydrogen bonds between the amine and carbonyl groups of the backbone [57]. Rather, the helical nature of the decapeptide is likely due to kinks along the protein backbone introduced by the proline residues, which restrict the dihedral angles available to the remaining amino acids. Sedimentation velocity experiments suggest that within each decapeptide, there are alternating stiff and flexible regions [10]. This semiflexible rod conformation has been adopted as a consensus model for the secondary structure of mfp-1.

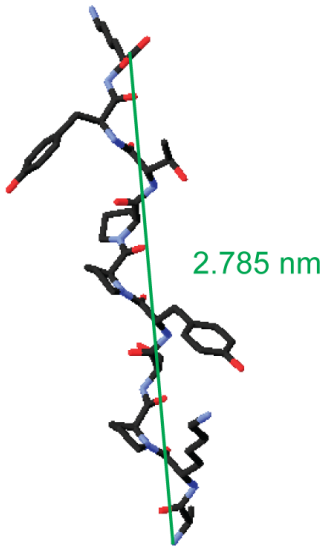

Figure 3.5: Helical secondary structure of the mfp-1 decapeptide. Constructed using SwissPDB Viewer[22] based upon the ϕ, ψ angles of the decapeptide in H_2O, as reported by Kanyalkar, *et al* [42].

Tertiary Structure

Due to the lack of driving forces for protein folding, the tertiary structure of mfp-1 adopts a random coil. The hydrodynamic radius of an mfp-1 monomer is 10.5nm [24].

3.1.2 Surface Adsorption

Adsorption Kinetics

Adsorption of mfp-1 onto surfaces occurs in a step-wise, multi-layer process [23, 25]. Prior to interacting with the surface, the proteins form aggregates in solution. A monolayer of these mfp-1 oligomers then forms on the substrate. After initial binding a conformational change occurs, indicated by a collapse in film thickness and an increase in surface coverage. Following this transformation, an ad-layer of mfp-1 is able to adsorb on top of the monolayer of protein covering the substrate.

Effects of pH

Solution pH determines the degree of aggregation of mfp-1 prior to adsorption, which in turn influences adsorption kinetics [23]. At high pH (6.5), larger hydrodynamic radii have suggested higher degrees of intermolecular association than were detected at lower pH (4.5). This effect may be due to the auto-oxidation of mfp-1 at high pH, resulting in crosslinking. This behavior will be discussed in detail in Section 3.1.3. Ad-layer formation follows the same pH-dependence of aggregation behavior. Under more alkaline conditions, a higher propensity toward crosslinking correlates with increased rates of ad-layer addition than at lower pH.

Structure of Adsorbed Mfp-1

The structure of adsorbed mfp-1 is highly dependent on substrate chemistry. When adsorbed onto hydrophilic surfaces such as SiO_2, a rigid, tightly-bound film is formed [16]. In contrast, on hydrophobic surfaces such as methyl-terminated solids, the protein molecules are extended as fully hydrated brush-like polymers. The mfp-1 films adsorbed on nonpolar surfaces are over three times as thick as comparable films on polar substrates.

The collapse of mfp-1 films on hydrophilic surfaces is likely due to the prevalence of polar residues which are able to form many hydrogen bonds with the substrate. This same characteristic of high hydrophilicity accounts for the extended and hydrated nature of mfp-1 on hydrophobic surfaces. Only two hydrophobic side chains (Ala1, Pro3) are able to favorably interact with the nonpolar substrate. The eight remaining hydrophilic residues of the decapeptide avoid the substrate, and instead interact with the surrounding water molecules. This result is supported by angle resolved x-ray photoelectron spectroscopy, which has demonstrated low energetic interactions with the substrate of mfp-1 adsorbed on poly(octadecyl methacrylate) [3, 4]. On POMA substrates, dehydrating the protein film results in substantial collapse and vertical and lateral aggregation of the adsorbed layer. The driving force for mfp-1 adsorption on hydrophobic surfaces is likely the displacement of bound water molecules at the interface of the nonpolar surface with the solvent.

Simulations and experiments have been performed to predict the orientation of the mfp-1 decapeptide to a variety of surfaces. Modeling of a decapeptide adsorbed on a Ge substrate indicates that the primary residue at the interface is DOPA [57]. The decapeptide is turned in such a way that the Tyr in the fifth po-

sition of the decapeptide is also oriented to the surface to stabilize the adsorbed film. The two hydroxyproline residues in the sixth and seventh locations position the DOPA side chain to optimally interact with the surface.

Adsorbed onto Au, as with decapeptides adsorbed onto Ge surfaces, the Pro residues are responsible for orienting the DOPA groups. DOPA on its own lies parallel to the Au surface [83], however with the two Pro residues neighboring the DOPA in recombinant decapeptide fragments, the DOPA ring is tilted to be nearly perpendicular to the Au surface [1].

Three features of mfp-1 appear to determine the adsorption behavior of mfp-1 and its constituent decapeptide onto surfaces: (1) The high ratio of polar to nonpolar amino acids, resulting in a strong dependence on substrate chemistry, (2) The presence of DOPA, which directly forms adhesive bonds with the surface, and (3) The role of the other residues in orienting the DOPA groups into their optimal conformation relative to the surface.

3.1.3 Crosslinking

The DOPA residues in mfp-1 are able to engage in crosslinking interactions, which are crucial for the mechanical and cohesive properties of this protein. Two types of DOPA-mediated crosslinks have been detected in the byssus:

1) Covalent DOPA-DOPA links, which form following the oxidation of DOPA residues (Figure 3.1.3A) [50],[5] [79].

2) Complexation with metal cations, such as Fe^{3+} (Figure 3.1.3B) and Cu^{2+} [72],[71],[84].

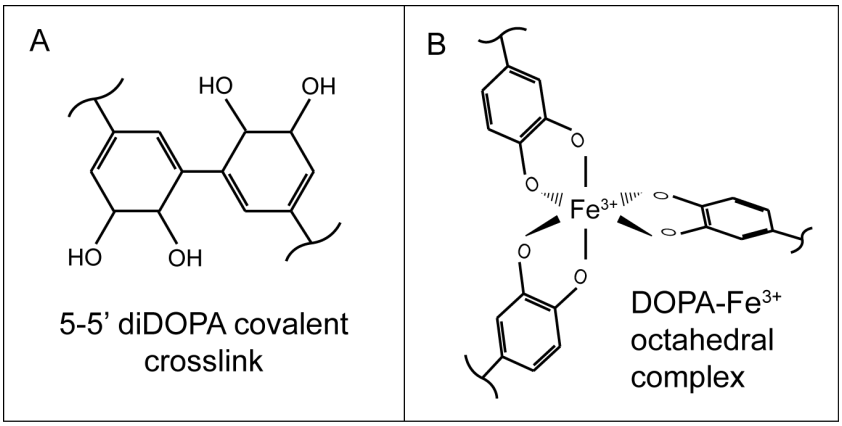

Figure 3.6: (A) Covalent 5,5′-diDOPA crosslink. (B) Octahedral coordination of Fe^{3+} by three DOPA groups.

Covalent crosslinking

In the byssus, the oxidation of DOPA residues to DOPA-quinone is mediated by a catechol oxidase enzyme [6, 79]. This process has been replicated in the laboratory using small molecule oxidizers such as $NaIO_4$ [5, 35, 69, 88] and H_2O_2 [31, 88]. Formation of these crosslinks varies for each thread and appears to be directly dependent on the attachment strengths needed to secure the mussel. During byssus formation under conditions of high shear flow, higher amounts of covalent crosslinks have been detected [50].

Initially, it was expected that following oxidation, DOPA would undergo a Michael-type addition with the amino groups on Lys residues from the decapeptide [80], however there is no direct evidence for the existence of these crosslinks. Furthermore, neither chemical nor enzymatic oxidation of DOPA influence the availability of Lys to bind alginate adlayers with an affinity for ϵ-amino groups [69]. Rather, as a result of spectroscopic evidence [50], a consensus has been reached that DOPA oxidation results in the formation of 5,5′-diDOPA crosslinks between carbon atoms in the catechol rings. It has been pro-

posed that two DOPA quinones, transformed into radical semiquinone species, could covalently bond via aryl-aryl coupling [5, 89]. A definitive reaction pathway for crosslink formation following oxidation of DOPA, however, has yet to be proven.

Ionic crosslinking

In addition to forming covalent crosslinks, metal coordination bonds are necessary for the mechanical robustness and internal cohesion of the proteins in the byssus. DOPA-containing mfp's are selective as to which ions can be used for crosslink formation [53]. Compared to a library of 18 metals in various oxidation states, Fe^{3+} and Mn^{3+} have been shown to form the highest number of crosslinks, followed by Cu^{2+} and Ag^{+}. Other oxidation states of these metals, as well as other period 4 transition metals (Ti, V, Cr, Co, Ni, and Zn), were unable to promote crosslinking of byssal proteins, even though in other contexts they are able to undergo coordination chemistry. Higher degrees of crosslinking could be achieved through the addition of oxidizing salts, and combinations of coordinating ions with oxidizers showed more crosslinking than either species on its own, suggesting that both types of crosslinks can coexist [31]. No group I or group II ions have been shown to cure mfps.

Formation of such metal crosslinks is a reversible and time-dependent process. Using the surface forces apparatus (SFA) to measure cohesion between two mfp-1 films, addition of small amounts of Fe^{3+} resulted in large pull-off forces between the protein layers [90]. With longer contact times, even higher cohesion was observed, and these contacts could be re-formed after the surfaces were separated.

Metal crosslinks play an important role in the mechanical properties of the mfp-1 cuticle. Isolated granules, rich in DOPA-Fe^{3+} chelates, have been identified throughout this layer [28]. Chemical removal of ions lowers the hardness of the cuticle by 50% while contributing to its degradation[34]. Phase separation of these hard regions of DOPA-Fe^{3+} complexes allows for inhomogeneous strain distributions throughout the cuticle, resulting in increased fracture toughness and extensibility [33]. Above 30% strain, microcracks have been observed in the metal complex-deficient matrix surrounding the granules, however they are prevented from propagating to catastrophic failure until the threads have reached 70% strain. In species of mussels which do not sequester ions into granules, such as *P. canaliculus*, failure of the cuticle begins at the onset of crack formation, also at 30% strain.

Viscoelastic properties

Rheological experiments have investigated the effects of crosslinking on mfp-1 [16, 29, 35], as well as combined gelatinous extracts of mfp-1 and mfp-2 [31, 53]. Crosslinking leads to stiffening of the protein matrix, as evidenced through release of coupled water, its subsequent collapse to a thinner matrix, increased shear modulus and viscosity, and decreased compressibility. These effects are more pronounced for oxidation-induced crosslinks than for metal complexation.

3.1.4 Surface Forces Apparatus Experiments

Experiments with the surface forces apparatus (SFA) have shown that the adhesion of mfp-1 can be altered by external factors. Adsorbed onto mica, non-adhesive films of mfp-1 were switched to become adhesive after mechanical shear was applied [48]. Using the analogous protein from a different mussel species (*Mytilus californianus*) it was shown that adhesion of mcfp-1 to mica could be increased at lower ionic strengths, and that most of the adhesion was lost when the protein was oxidized [49].

In this work, we have investigated the effects of chemical crosslinking on the adhesion of mfp-1. In nature, inter- and intramolecular mfp-1 crosslinks are mediated by boning between DOPA residues- the same sidechains responsible for adhesion. Here, we hypothesize that by forming crosslinks, fewer DOPA residues will be able to participate in adhesion and superficial adhesion will decrease. Meanwhile, crosslinking will strengthen the cohesion among the proteins, and the stiffness of mfp-1 films will increase. Films of mfp-1 from *M. edulis* were crosslinked ionically, via Fe^{3+} ions, and covalently, following oxidation promoted by $NaIO_4$. Adsorption, adhesion, and stiffness of mfp-1 in these states was measured in the AFM.

CHAPTER 4

MATERIALS AND METHODS

4.1 Atomic Force Microscope

4.1.1 Instrumental Design

The atomic force microscope (AFM) is a member of the scanning probe microscope family. A schematic illustration of the instrument is shown in Figure 4.1. At its core, the AFM consists of a tip mounted onto the end of a compliant cantilever, with a laser beam reflected off of its back edge. As the tip interacts with the sample surface, bending of the cantilever results in a proportional shift in the path of the laser reflection. Changes in the laser position are detected in a four-quadrant photo-sensitive detector (PSD), or photodiode. The PSD measures normal bending of the cantilever through vertical changes in laser position, and measures torsional bending through lateral changes in the laser spot.

The movements of the cantilever are controlled by three piezoelectric actuators which move the base of the cantilever in the x, y, and z directions. These scanners are equipped with closed-loop sensors to accurately detect their positions.

4.1.2 Imaging

Images of the surface are generated in the AFM by raster scanning across a predefined area. This can be accomplished in a number of ways, two of which

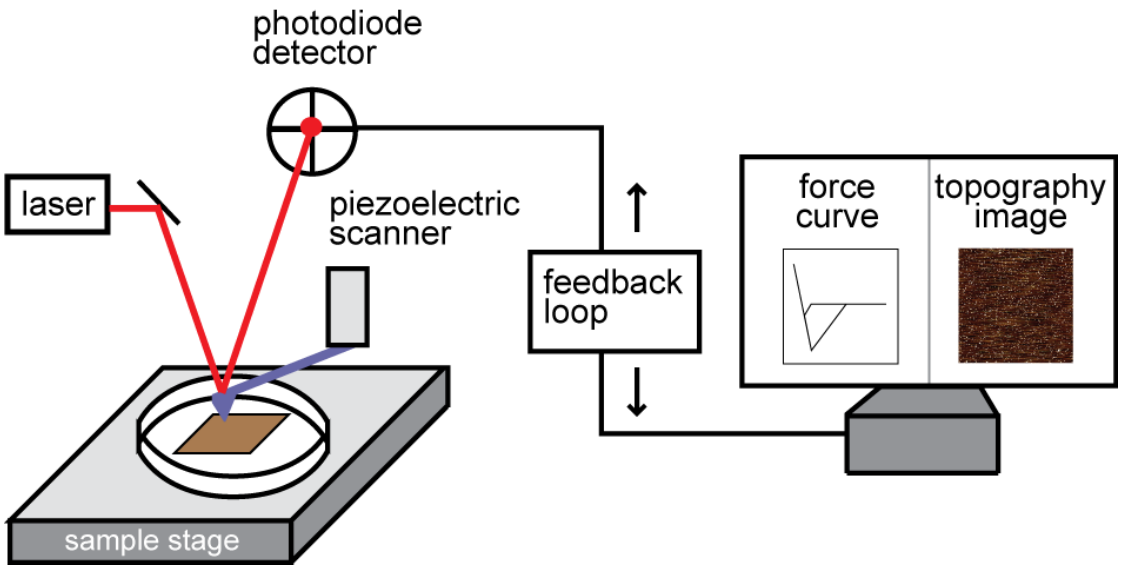

Figure 4.1: Components of the AFM.

were used in this work: (1) Contact mode, in which the tip is brought directly into contact with the sample for the duration of the scan, and (2) Tapping mode, in which the cantilever oscillated at a frequency near its resonance and intermittently contacts the surface as it scans. The imaging mode selected for each surface was dependent on sample properties.

In contact mode scanning, as the name implies, the tip is in direct contact with the sample for the entire scan. A feedback mechanism between the computer and the hardware adjusts the height of the piezos to maintain a constant deflection. A topography image is built from the changes in piezo extension. A friction image of the torsional bending of the cantilever and a raw deflection image are collected in parallel. DNP-S probes (Bruker, Camarillo CA) were used for contact mode imaging, with triangular silicon nitride cantilevers, k=0.06N/m or 0.12N/m, and a silicon tip with a radius of 10nm.

In tapping mode, the cantilever oscillates at a frequency slightly below its

resonance to make short, frequent contacts with the surface. This method is particularly useful for soft and biological samples because it does not allow the tip to drag material with it as it scans the surface. Additionally, the high velocity of the tapping typically results in stiffening of viscoelastic materials, increasing the resolution of the image. The feedback loop in tapping mode maintains a constant tapping amplitude, and moves the piezos closer or farther from the surface to do so. In addition to the topography image, amplitude and the phase images are generated. The amplitude image gives an indication of the elasticity of the sample, while the phase gives its damping properties.

In this work, magnetic AC mode is used, in which a magnetic thin film has been deposited on the back of the cantilever, and a magnetic actuator is used to oscillate the cantilever. This method reduces mechanical vibrations. It also maintains a strong, well-defined resonance frequency, which is particularly important in fluid where damping is high. Type VI MAC levers (Agilent Technologies, Santa Barbara CA), with a spring constant of 0.2N/m, a triangular silicon nitride cantilever, and a silicon tip with a radius of 10nm.

To improve the quality of the image, three user-defined parameters were varied, depending on the imaging mode: (1) Setpoint. This determines the deflection, if in contact mode, or tapping amplitude, if in tapping mode, that the feedback loop will maintain. This parameter determines how hard the tip is pressing on the sample: at a higher deflection or lower amplitude, the tip will apply a greater load to the surface. The setpoint is significant only relative to the deflection or amplitude out of contact. (2) Scan speed. If the scan speed is too low, there will be dragging, and if the scan speed is too high, features will be missed and streaking will be observed. In contact mode, scan speeds were

typically 0.5-1 lines/s, and in tapping mode, speeds were typically 1-2 lines/s. (3) Integral (I) and proportional (P) gains of the feedback loop. These parameters determine the response rate of the feedback loop. At high gains, images are very noisy, whereas at low gains, images lack resolution. In the images presented here, I values of 1-5% were used, and P values were two times I, from 2-10%.

Data Analysis

Data analysis was performed using a combination of three software packages: PicoView 1.8 (Agilent), Gwyddion, and MATLAB (Mathworks). Processing images was performed using four features of Gwyddion: (1) Leveling data by mean plane subtraction, (2) Removing polynomial background, (3) Correcting lines by matching height median, and (4) Correcting horizontal scarring. The first two of these tasks were performed in order to flatten the background of the image. The background of raw AFM topography images are typically distorted due to the nonlinearity and creep behavior of the piezoelectric actuators. This often takes the shape of a second or third degree polynomial, and further leveling, as well as removal of sample tilt, was performed through mean plane subtraction. The degree of the background polynomial was selected through a visual inspection of each image. Further processing improved the clarity of images by removing mismatches in height between neighboring horizontal scan lines, and removing streaking from topographical features.

Two quantitative pieces of information were derived from these images. The root-mean-square (RMS) roughness of the films was calculated using Gwyddion according to the following equation:

$$RMS = \sqrt{\frac{1}{n}\sum_{i=1}^{n} z_i^2} \tag{4.1}$$

where n is the number of data points, and z is the height of each pixel.

To describe the distribution of features in the images, average peak-to-peak distances were calculated using MATLAB. These values were calculated over each horizontal scan line, and averaged for the total area of the film. Peaks were defined as the maximum of the four points in the horizontal scan line preceding and following the peak. A minimum threshold for peak height was imposed at 1nm above the minimum height of the given scan line.

4.1.3 Force Curves

Normal forces between an AFM tip and a sample are measured by performing vertical sweeps to bring the tip into contact with the sample and pull it back from of contact. From the vertical deflection of the cantilever, a force-distance profile is built to quantify adhesive and mechanical properties of the sample.

An AFM force curve can be split into five regions as shown in Figure 4.1.3:

(1) A non-interacting interval, in which the tip is above the sample. Here, deflection remains constant as the tip approaches the sample.

(2) A jump-into contact, in which attractive forces pull the tip down toward the sample

(3) A repulsive regime, in which a compressive load is applied to the sample.

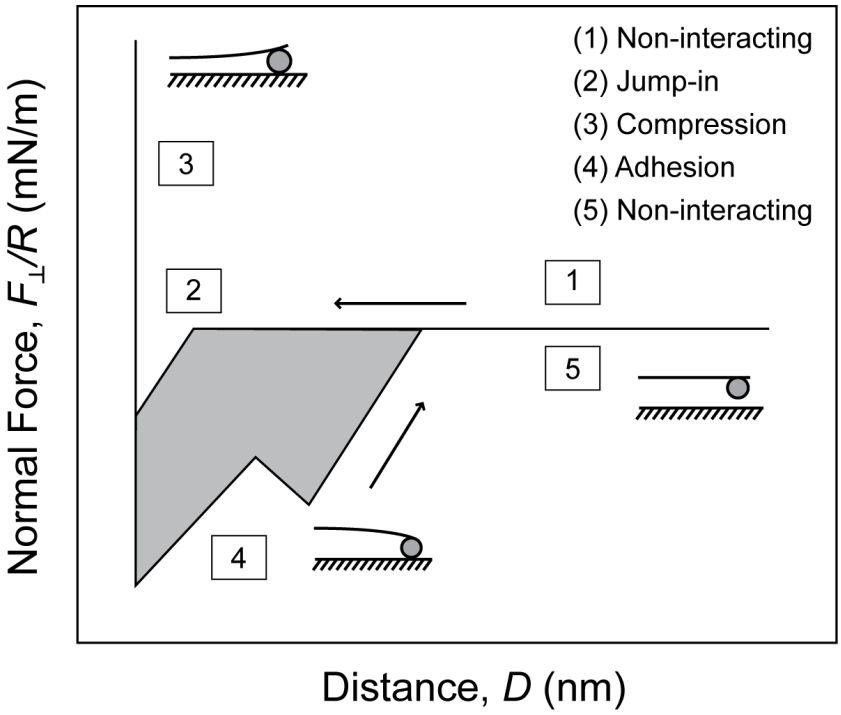

Figure 4.2: Schematic of a force curve.

(4) An adhesive regime, in which adhesive forces pull down on the tip before it is separated from contact.

(5) A second non-interacting region following the separation of the tip-sample interface. As in (1), the deflection remains constant as the cantilever returns to its original position.

Colloidal Probe Microscopy

The colloidal probe technique, first demonstrated by Ducker *et al* [14], was used to collect force curves. Rather than using a sharp tip, such as those used for imaging, a spherical particle is glued onto the end of the cantilever. This shape has a large, well-defined, and tunable area of contact. The large tip size mod-

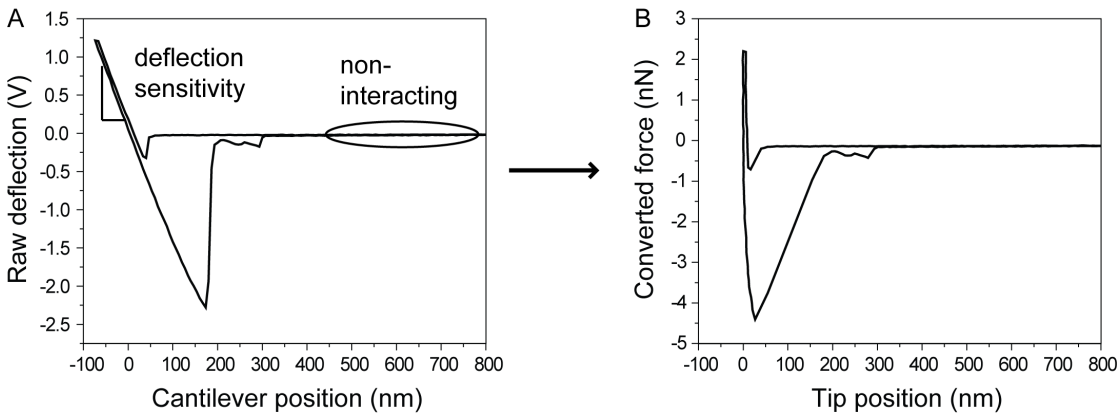

Figure 4.3: Conversion of force curve data from (A) raw deflection vs. cantilever position to (B) Normal force vs. tip position.

erates the amount of pressure that can be applied by the tip on the surface, lowering the risk of distortion and damage to the sample. Furthermore, knowledge of the tip's shape allows the Derjaguin approximation to be applied when modeling the data using contact mechanics (Section 2.2).

The force curves in this work were all collected using the colloidal probe technique. Silica spheres, radius 300nm, were mounted on triangular silicon nitride cantilevers, with spring stiffness 0.03N/m (Novascan Technologies, Ames IA).

Conversion of Raw Data

Raw AFM data is recorded as the position of the vertical piezo at the base of the cantilever (Z_p) vs. the voltage of the deflected laser beam in the PSD (V). For meaningful interpretation of the results, these quantities were converted into the force of the normal interaction between the tip and the cantilever (F), and the distance between the AFM tip and the surface (D)[7] (Figure 4.3).

To convert V into F, the normal bending of the cantilever is treated as a Hookian spring to follow the relation $F = kx$, where k is the spring constant of the cantilever. The change in position of the laser spot in the PSD is directly proportional to the vertical deflection Z_c of the cantilever. This proportionality between voltage and distance was calculated from the high compressive load regimes of the force curves. Where V vs. Z_c is linear, an assumption is made that the tip does not continue to indent into the sample. Rather, the change in deflection is considered exclusively the result of cantilever bending. The slope of this region, m, is the inverse of the deflection sensitivity, and gives this proportionality between the photodiode readings and the physical distance of cantilever bending. The normal force of the interaction can then be calculated by $F = mkZ_p = kZ_c$.

To convert the measured position of the base of the cantilever to the tip-sample separation distance, the position of the cantilever is added to the deflection of the cantilever: $D = Z_c + Z_p$.

Converted force curves were shifted to a reference point at (F,D) = (0,0). F=0 was defined by the mean of the final 100 points in the force curve, which are found in the non-interacting regime of the retraction. D=0 was defined at the point in the retraction of the cantilever at which the force was closest to zero.

Adhesion

Zero force was defined as the raw force read by the photodiode when the tip is not interacting with the sample, therefore all negative forces were considered adhesive. All thresholds were taken at integer multiples of the noise in the

forces of the non-interacting regime, taken as the standard deviation (σ) of the points which were averaged to give zero force. The thresholds were selected to not over- or under-select adhesive minima.

During the approach of the tip toward the surface, it was important to know not only the force at the minimum, but also where the jump-into contact began. The beginning of the jumpin was selected by the first point on the approach curve 5σ below F=0. The end of the jumpin was set as the global minimum of the approach curve. The jumpin force was reported as the force value of the end of the jumpin. The distance of the jumpin was taken as the distance between the data point preceding the onset of the jumpin (i.e. the last data point in the non-interacting regime), and the position of the end of the jumpin.

During the retraction, each local minimum in force was considered to be a jumpout event. To distinguish the local minima from noise in the data, a threshold was selected as 3σ in force below the point preceding and the point following the jumpout.

Elastic Modulus

Elastic modulus was extracted from the retraction of the force curves. The JKR model was fit to these force curves based on theory and equations discussed in Section 2.3.2. The results of this modeling were highly sensitive to the conversion of the raw data into forces. When converting raw data, an assumption was made that at high compressive load, the linear force-distance resulted exclusively from cantilever bending, with no further indentation of the tip into the sample. This imposes a ”hard wall” effect, which is clearly observed when

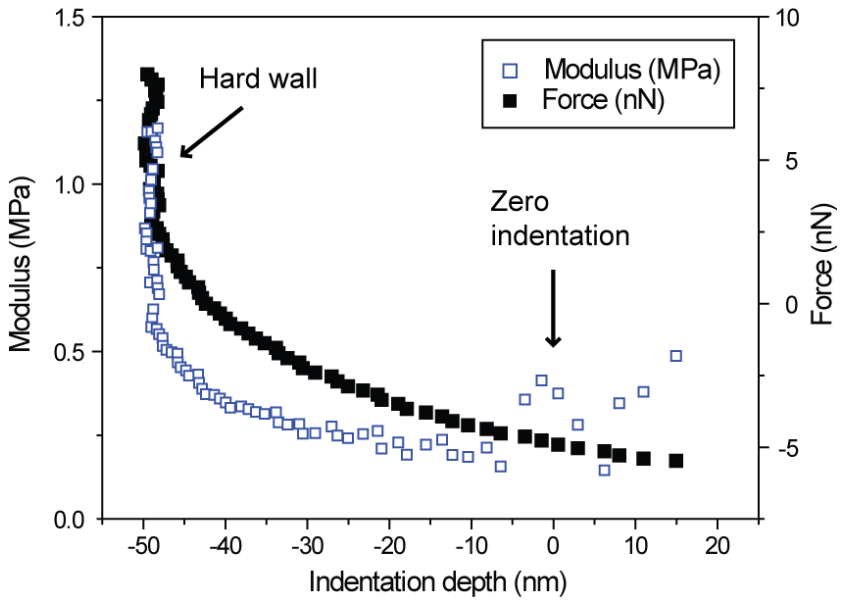

Figure 4.4: Modulus (blue) calculated as point-by-point fit along force curve (black).

looking at a point-by-point fit of the JKR model and the back-calculated modulus values (Figure 4.4).

Force curves with a higher adhesive load travel over a larger indentation before the surfaces separate. In order to maintain a consistent range across all force curves, the modulus was calculated from JKR fits between the hard wall and 10nm removed from the hard wall.

Calibration of Photodiode Nonlinearity

The photodetector in the AFM used is linear only from approximately -5V to +5V. To maximize the useable range of the detector, the nonlinearity of the detector was calibrated, so the force could be extrapolated. For the calibration, the base cantilever deflection was aligned as low as possible in the photodiode, between -9.5 and -10V. Force curves were collected on a rigid glass slide, and were

taken to their saturation at +10V. These curves were fit to a sum of sines with two terms:

$$V = a_1 sin(b_1 x + c_1) + a_2 sin(b_2 x + c_2). \tag{4.2}$$

This calibration was performed for each cantilever used.

4.2 Surface Forces Apparatus

The surface forces apparatus (SFA) is a complementary tool to the AFM. The configuration of this instrument is shown in Figure 4.2 [39, 38, 37]. The SFA measures the normal force between two silica cylinders, radii 1-2cm. The cylinders are arranged in a crossed configuration, and mounted on double-cantilever springs. Thin, freshly cleaved sheets of mica are glued to the cylinders, and a layer of Ag is deposited onto the backs of the mica sheets.

Forces are measured in the SFA using multiple beam interferometry. The interferometer is built by shining white light through the cylindrical disks. The light reflects between the Ag films deposited on the mica surfaces, and only light at wavelengths which constructively interfere is transmitted. A spectrometer splits the transmitted light into its component wavelengths as fringes of equal chromatic order (FECO), which are recorded by a charge-coupled device (CCD) camera. The wavelengths are calculated relative to reference Hg spectral lines. The positions and shapes of the FECO fringes are used to calculate the shapes of the surfaces and the distance which separates them.

Mfp-1 in solution was deposited onto mica surfaces in a symmetric con-

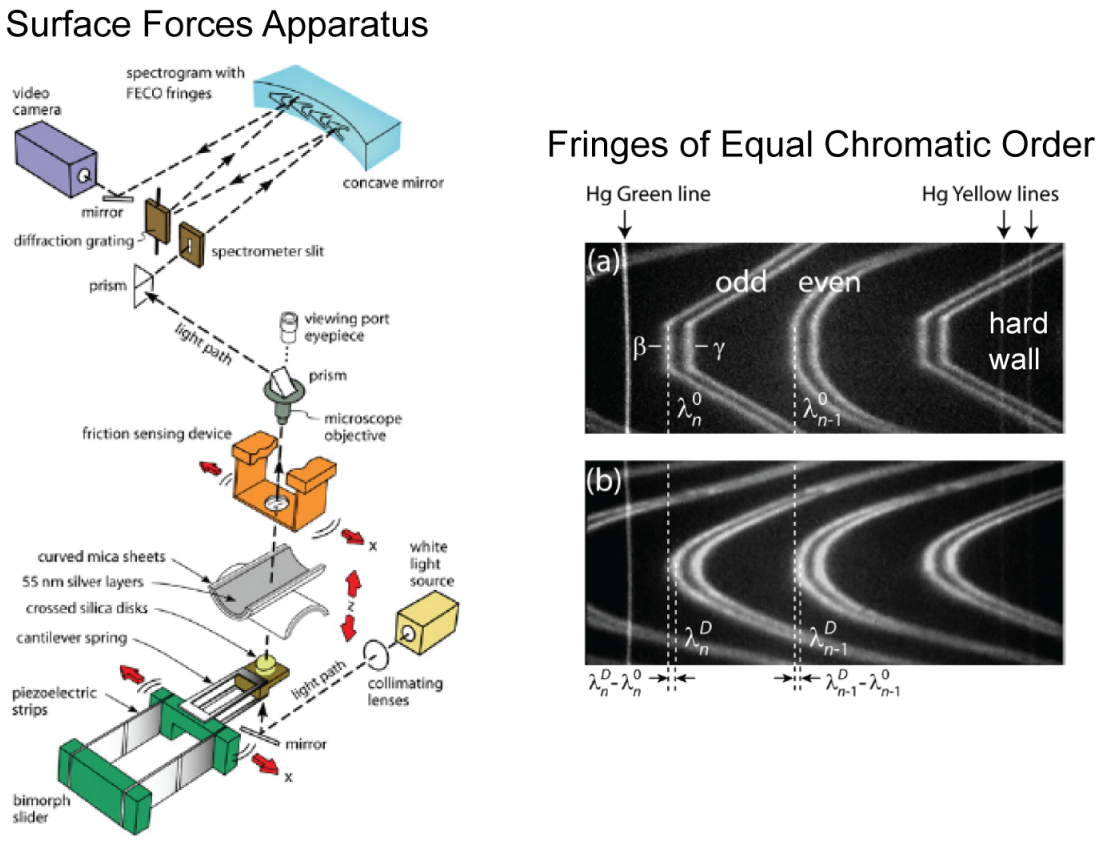

Figure 4.5: (Left) Instrumental design of the surface forces apparatus. (Right) Raw FECO fringes. Adapted from [37].

figuration. Droplets of mfp-1 were added with the surfaces mounted in the instrument, and separated to a large, macroscopic distance to ensure that the molecules on each film could not form entanglements with the opposing film.

4.3 Mfp-1 Sample Preparation

Mfp-1 was extracted from the foot glands of *Mytilus edulis* by the laboratory of Dr. J.H. Waite (Marine Biology, UC Santa Barbara) according to published methods [81]. Purified powders were dissolved in acetate buffer, pH 5.5, con-

taining 0.1M sodium acetate and 0.25M potassium nitrate to a concentration of 250 μg/mL, and subsequently diluted to 37.5 μg/mL prior to deposition. Mfp-1 powders were stored at -80°C, and solutions were stored at -20°C, all in light-free environments. To prepare the protein films, 250μL of dilute mfp-1 solution were deposited onto freshly cleaved mica and incubated for 1 hour in a light-free environment. Following the adsorption period, films were gently rinsed three times with buffer. To mimic the *in vivo* enzymatic oxidation-induced formation of covalent crosslinks, 1mM $NaIO_4$ in buffer was added to mfp-1. Metal cations were introduced with 10μM $FeCl_3$ with 1mM tris in buffer. All crosslinkers were added following adsorption of mfp-1, and directly prior to mounting samples for experiments in the AFM. All sample preparation was performed in a laminar flow cabinet.

CHAPTER 5

RESULTS

5.1 Characterization of Crosslinking at Mfp-1 Film Surfaces

5.1.1 Thickness

To confirm the adsorption of mfp-1 to mica, SFA force-distance curves were collected to measure the thickness of the protein films in buffer. A force-distance profile of mfp-1 recorded by the SFA is shown in Figure 5.1. The equilibrium thickness of one mfp-1 film was 37.6nm, and the fully compresed (hard-wall) thickness was 10.2nm. The equilibrium thickness of 37.6nm is approximately three times the hydrodynamic radius of a single mfp-1 molecule (10.5nm[24]), and indicates that a multilayer protein film has adsorbed to the mica.

5.1.2 Morphology

Different morphologies of mfp-1 films in buffer, Fe^{3+}, and $NaIO_4$ were observed through topography images of the surfaces (Figures 5.1.2,5.1.2,5.1.2 respectively). RMS roughness and lateral peak-to-peak distances were computed to quantify the distributions of proteins on each surface, and both average values are reported in Table 5.1. In buffer, a protein film fully covered the mica substrate, and isolated, tall globules rested on top of this film. The surfaces of the films in buffer were the roughest. In Fe^{3+}, globules were shorter and narrower than those in buffer, and they fully covered the surface. When imaged in

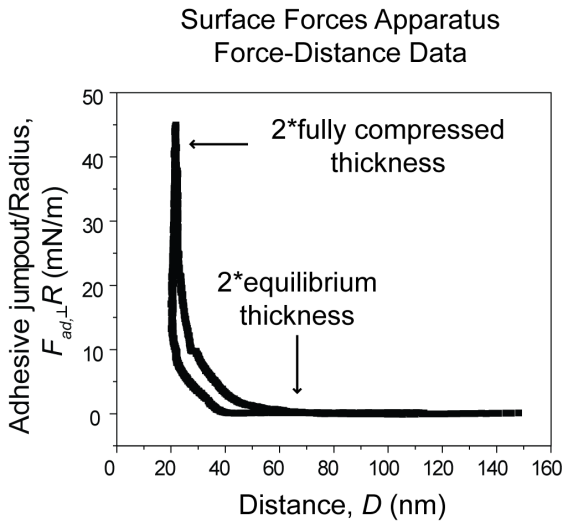

Figure 5.1: Force-distance curve taken in the SFA.

contact mode, the images of the films in buffer were characterized by horizontal streaking, decreased roughness, and flattening at the scan edge (Figure 5.1.2. This suggests that material was being dragged across the surface of the film by the AFM tip.

The films in Fe^{3+} were the least rough. In $NaIO_4$, a different type of morphology was observed. Unlike the globules present in buffer and Fe^{3+}, mfp-1 surfaces with $NaIO_4$ contained a network of pores. The heights of the pores and the overall film roughness were intermediate, between the average globule heights and the RMS roughnesses in the other two cases. The lateral spacing between peaks was the smallest for the $NaIO_4$ surfaces. With Fe^{3+} or $NaIO_4$ present, there was no evidence that material from the protein films was dragged across the surface as in buffer. Compared to mfp-1 films in buffer, the surfaces with Fe^{3+} and $NaIO_4$ crosslinkers were more dense, more cohesive, and the protein was more uniformly distributed throughout the films.

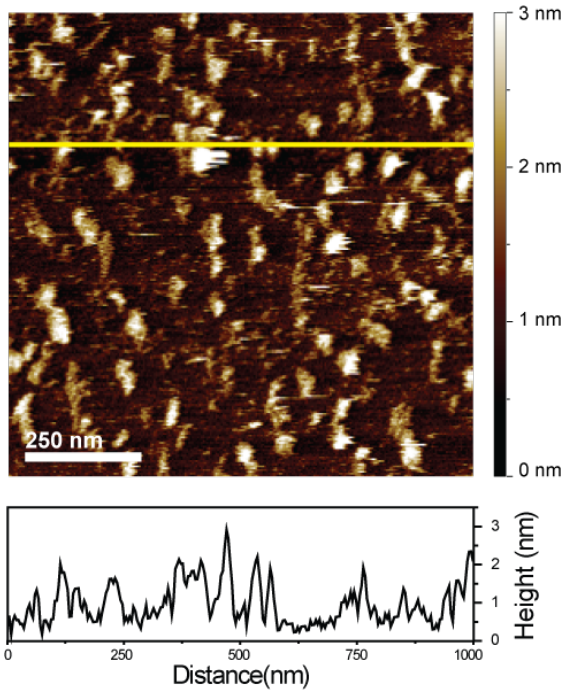

Figure 5.2: Topography of non-crosslinked mfp-1, imaged in tapping mode. Image size is 1x1 μm.

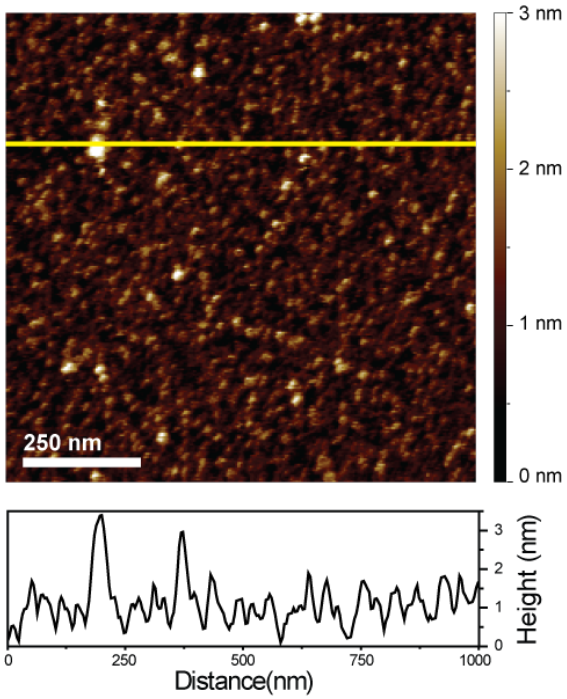

Figure 5.3: Topography of mfp-1 crosslinked with 10μm Fe^{3+}, imaged in contact mode. Image size is 1x1 μm.

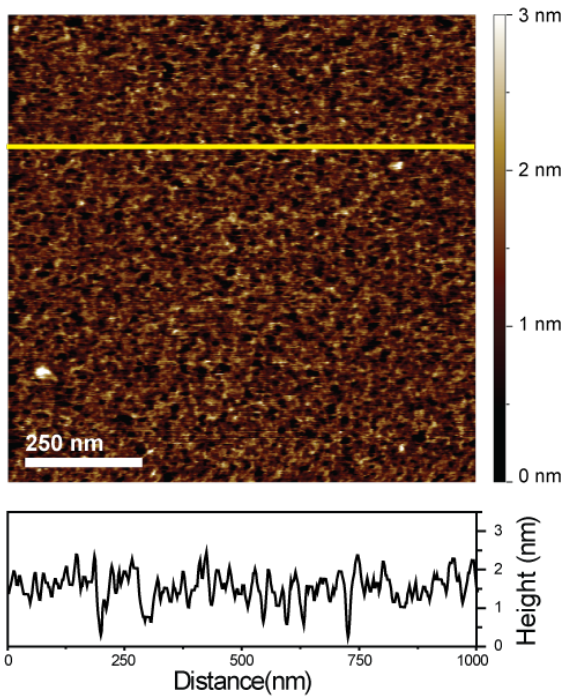

Figure 5.4: Topography of mfp-1 crosslinked with 1mM $NaIO_4$, imaged in contact mode. Image size is 1x1 μm.

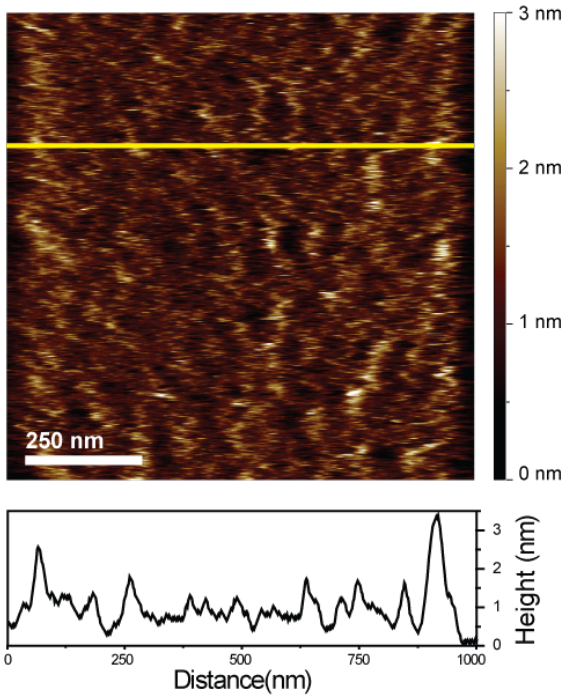

Figure 5.5: Topography of non-crosslinked mfp-1, imaged in contact mode. Image size is 1x1 μm.

Condition	RMS roughness (nm)	Peak-to-peak distance (nm)
Buffer (TM)	0.82 ± 0.31	72 ± 45
Buffer (CM)	0.67 ± 0.51	50 ± 32
Fe^{3+}	0.450 ± 0.002	58 ± 34
$NaIO_4$	0.49 ± 0.04	26 ± 11

Table 5.1: RMS roughness and peak-to-peak distances for topography of non-crosslinked and crosslinked mfp-1 films. All values are mean ± standard deviation.

	Elastic modulus
Buffer	0.69 ± 0.29 MPa
Fe^{3+}	1.18 ± 0.71 MPa
$NaIO_4$	1.15 ± 0.76 MPa

Table 5.2: Mean ± standard deviation of the elastic moduli of mfp-1 films calculated by fitting the JKR model to the retraction of the force curves.

5.1.3 Stiffness

Calculated values of stiffness are shown in Tabel 5.2. Mean stiffnesses of the mfp-1 films were 71% higher in Fe^{3+} and in $NaIO_4$ than they were in buffer. The increased stiffness resulting from the addition of Fe^{3+} and $NaIO_4$ supports the indications from the film topography that intermolecular crosslinks have formed under these conditions.

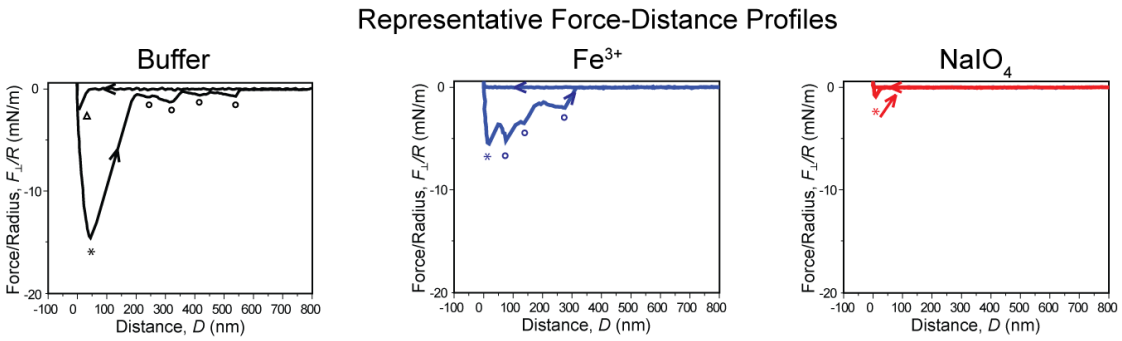

Figure 5.6: Characteristic force-distance curves of mfp-1 in buffer (black), Fe^{3+} (blue), and $NaIO_4$ (red). The jump into contact, observed in buffer only, is indicated by a "Δ". The first jumpout, F_{ad}/R, is indicated by a "*". Subsequent jumpouts are indicated by a "o".

5.2 Adhesion of Crosslinked Mfp-1 Films

Characteristic force profiles for mfp-1 in buffer, Fe^{3+}, and $NaIO_4$ are shown in Figure 5.6.

5.2.1 Attractive Jump-in

The mfp-1 films were able to spontaneously capture the opposing AFM tips in buffer, but they were not able to do so in Fe^{3+} or $NaIO_4$. Adhesive forces were measured up to 60nm above the film surfaces in the approach regimes of the force profiles in buffer (Figure 5.6, "Δ"). These attractive jumps into contact never occurred under either crosslinking condition. Rather, in Fe^{3+} and $NaIO_4$, purely repulsive profiles were exhibited during loading.

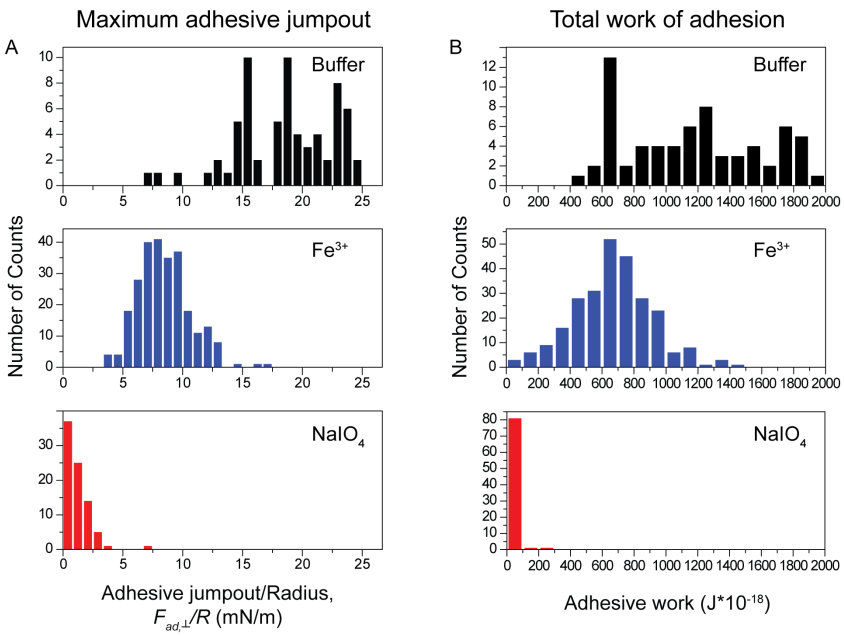

Figure 5.7: (A) Force of first pull-off event. (B) Total work of adhesion.

Pull-off Force

Adhesion of each mfp-1 film was quantified via the adhesive force, F_{ad}/R, and the total work of adhesion, ΔW. Throughout this section, adhesive forces reported are the first jumpout of the tip from contact with the surface (Figure 5.6, "*"). Work of adhesion was calculated from the difference in area between the approach and retraction curves ($\Delta W = W_{approach} - W_{retract}$). Both mean values of adhesion were higher for non-crosslinked mfp-1 (17.7mN/m, 1170J*10^{-18}), followed by moderate adhesion with Fe^{3+} crosslinks (8.5mN/m, 670J*10^{-18}), and finally $NaIO_4$, which demonstrated little to no adhesion (0.77mN/m, 49J*10^{-18}) (Figure 5.7). Interestingly, the distributions of adhesive work contained a common mode at 1200mJ/m^2 for mfp-1 in buffer and Fe^{3+}.

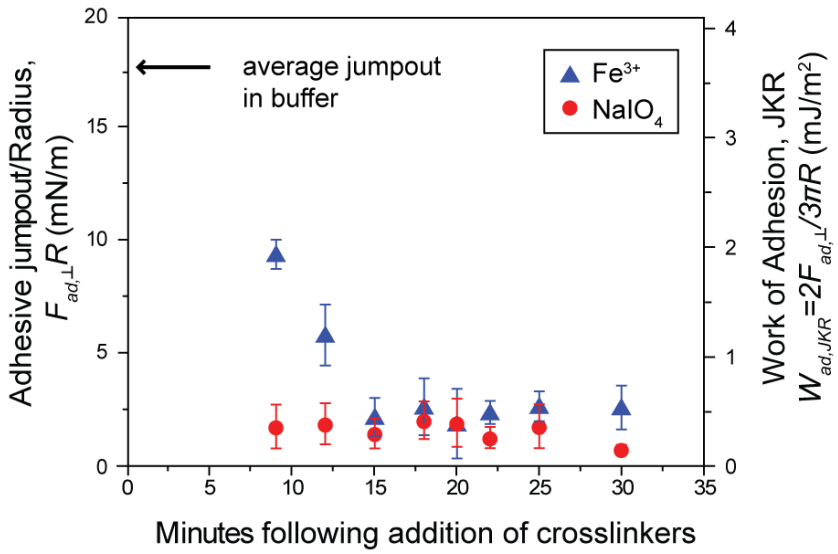

Figure 5.8: Adhesive force, measured as a factor of time following the introduction of crosslinkers to the mfp-1 film.

5.2.2 Kinetics of Crosslinking

Collection of force curves began as early as experimentally feasible, within 9 minutes following the addition of crosslinkers to the mfp-1 samples. After adding Fe^{3+}, the adhesive jumpout decreased with time, and stabilized after 15 minutes (Figure 5.8). With $NaIO_4$, by 9 minutes adhesion was lowered, and it remained within a consistent range throughout the course of each experiment. All other data reported in this work was measured after crosslink formation had reached a plateau.

5.2.3 Kinetics of Binding/ Unbinding

In order to determine whether the adhesion of mfp-1 is rate-dependent, the approach/retraction rate of the cantilever was modulated between 4μm/s, in

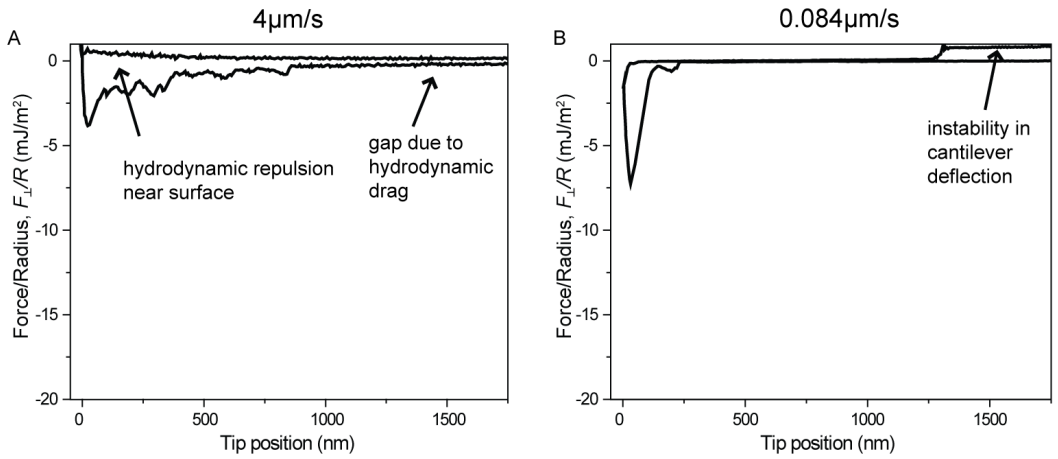

Figure 5.9: Limits in cantilever rates for (A) fast (4μm/s) rates, in which hydrodynamic forces lead to repulsion as the tip approaches the surface, as well as a hysteresis in the non-interacting force between the approach and retraction, and (B) slow (0.084μm/s) rates, in which instabilities were observed, often while the tip was out of contact.

which large hydrodynamic drag was observed, and 0.084μm/s, in which instability of the motion of the z-piezoelectric actuator began to interfere with reliable interpretation of some data sets (Figure 5.9).

In the approach regimes of the force curves, rate did not influence the capture force of the tip by mfp-1 in buffer, except at the fastest rate when the jump-in behavior was not observed (Figure 5.10). Rather, any interaction between the AFM tip and extended mfp-1 chains was masked by repulsive hydrodynamic forces as the cantilever neared the film surface. Changes in the approach rate did not enable spontaneous capture of the AFM tip in either crosslinked state.

In the tensile regime of the force curves, the rate had an influence on mfp-1 in buffer at the fastest rate, in which the adhesive jumpout was lower. At the slowest rate, adhesion was higher (Figure 5.11). Between these extremes, however, adhesive forces remained within a stable range. With the addition of

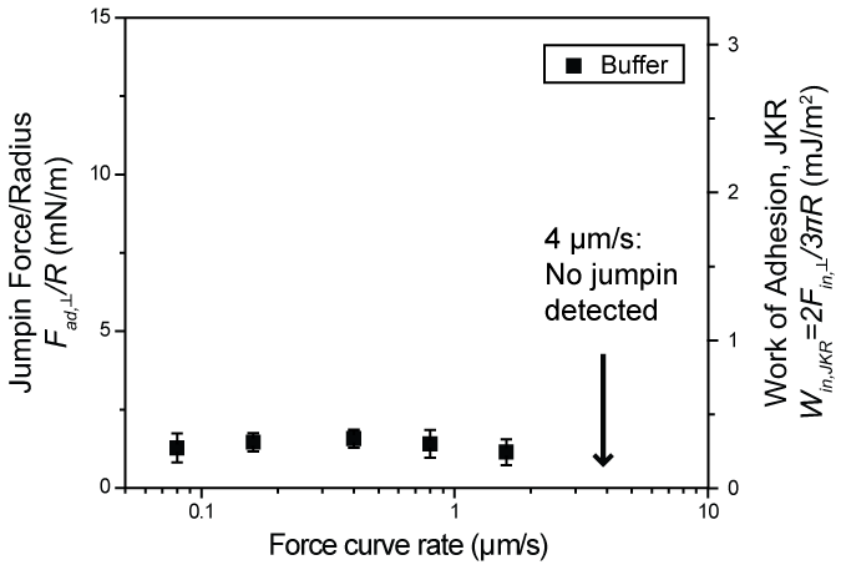

Figure 5.10: Effects of approach/retraction rate of AFM cantilever on (A) Jump-in to contact. Jump-in events were not observed at 4μm/s in buffer, nor in either crosslinked condition. (B) Maximum adhesive jumpout.

Fe^{3+} cations and $NaIO_4$, rate effects were not observed.

All other data reported in this work was measured at a rate of 0.8μm/s.

5.3 Long Range Adhesive Interactions

5.3.1 Extension of Individual Chains

In the non-crosslinked and Fe^{3+}-crosslinked films, long range (up to 1250nm) adhesive forces were also detected following the initial short-range jumpout. These adhesive interactions manifested as series of discreet separations between the tip and the protein films (Figure 5.6, "o"). Three quantitative parameters were extracted from this data: (i) the forces of the jumpouts, F_{ad}/R, (ii) the sep-

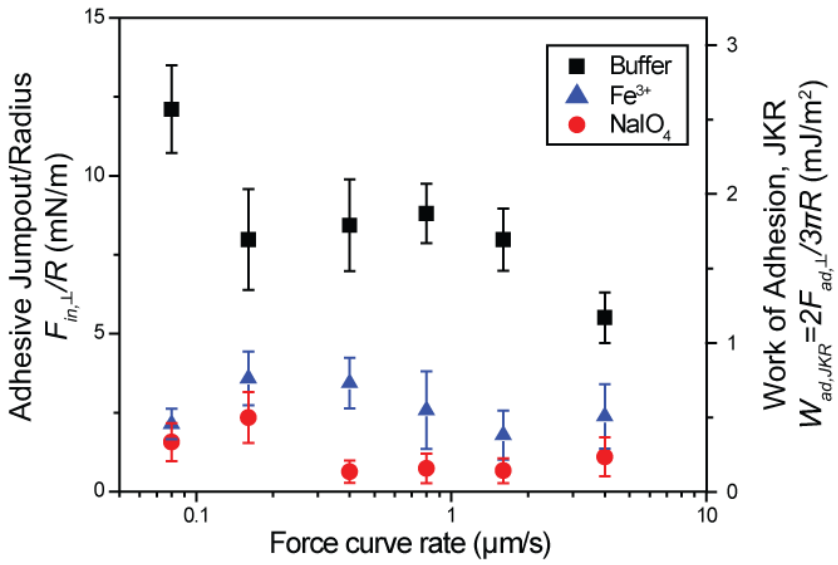

Figure 5.11: Effects of approach/retraction rate of AFM cantilever on (A) Jump-in to contact. Jump-in events were not observed at 4μm/s in buffer, nor in either crosslinked condition. (B) Maximum adhesive jumpout.

arations between the surfaces at each jumpoput, D, and (iii) the distances between sequential jumpouts, ΔD (Figure 5.12). In buffer, the jump-outs occurred at lower forces than the initial jumpout. In Fe^{3+}, the sequential jumpouts were at higher forces than in buffer, and they were often stronger than the initial F_{ad}/R. The separation between the tips and surfaces was longer in buffer than in Fe^{3+}. The distributions of ΔD contained a common mode for both buffer and Fe^{3+} centered at 37.5nm. In buffer, an additional mode was centered at 237.5nm. The separation events which contributed to this secondary mode primarily occurred between the first and second jumpouts.

Long-range bridging behavior was not observed following $NaIO_4$-induced crosslinking; rather, all adhesive contacts between the tip and these films were released with the initial separation of the surfaces.

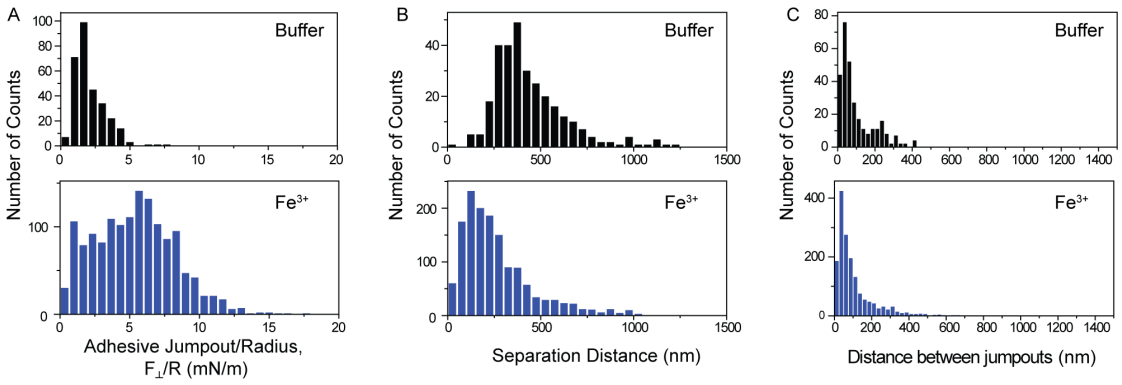

Figure 5.12: Adhesive jumpouts following the initial separation of the AFM tip from contact with mfp-1 in buffer (black) and Fe^{3+} (blue). (A) Pull-off forces of all subsequent jumpouts. (B) Distances until detachment of all subsequent jumpouts. (C) Distances between consecutive jumpouts. Multi-jumpout behavior was not observed in the presence of $NaIO_4$.

Single Attachment Strength of Mfp-1

For a more detailed look at the adhesive interactions of mfp-1 with the AFM tip, we compared the initial formation of adhesive bonds with their final release and separation in buffer. In this case, the first adhesive contacts were made during the spontaneous jump-in as the tip approached the film surface. The final separation event was the last long-range jumpout in each force curve.

Distributions of adhesive forces for these two quantities contained three distinct, common peaks (Figure 5.13). Means of each peak are summarized in Table 5.3, and are centered at multiples of approximately 0.2nN. These results suggest that mfp-1 formed adhesive bridges with the AFM tip via discreet attachments, each of which interacted with the SiO_2 sphere with an attractive force of 0.2nN.

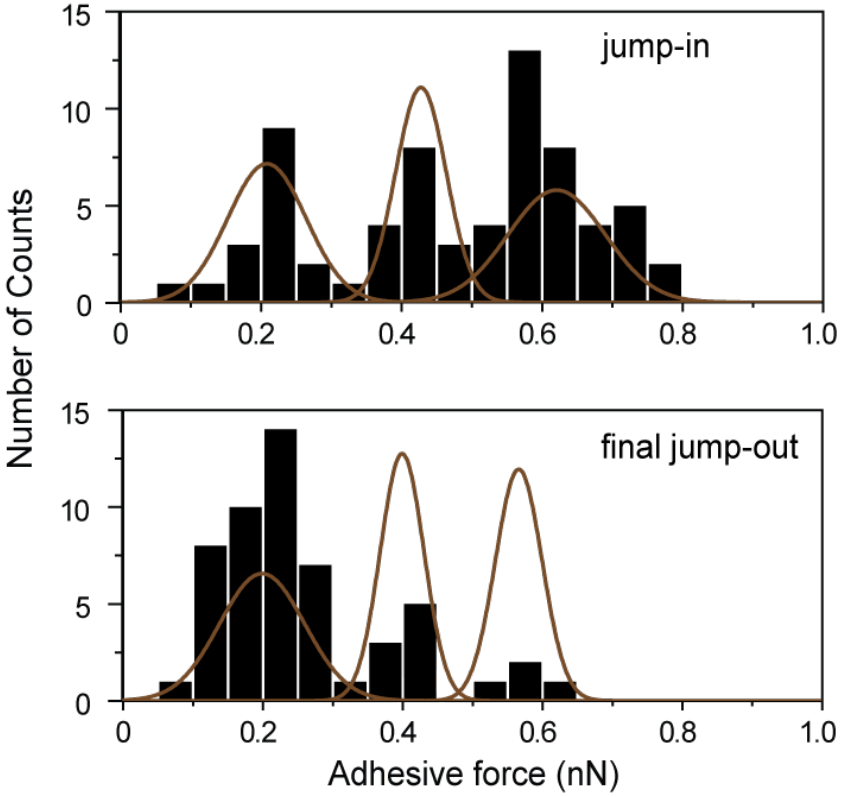

Figure 5.13: Forces of jump-in and jump-outs, with three matching peaks at multiples of 0.2nN.

	peak 1	peak 2	peak 3
jump-in	0.21 ± 0.06 nN	0.43 ± 0.04 nN	0.62 ± 0.07 nN
jump-out	0.20 ± 0.06 nN	0.40 ± 0.03 nN	0.57 ± 0.03 nN

Table 5.3: Mean ± standard deviation for each peak in the distribution of adhesive forces for the jump-into contact and the final jump-out from contact.

CHAPTER 6

DISCUSSION

The likely configuration of the superficial adhesive contact of mfp-1 with a foreign surface is shown in Figure 6.1. Without crosslinkers to cause the DOPA residues to bond with one another, many of these highly adhesive moieties were available to interact with the opposing AFM tip. The prevalence of non-bonded DOPA residues thus led to high adhesion in buffer. With Fe^{3+} and $NaIO_4$ added, fewer DOPA groups were present to interact with the surface, and adhesion decreased. This result with $NaIO_4$ is consistent with previous work using protein from *M. californianus*, which showed that adhesion of mcfp-1 to mica decreased with the addition of $NaIO_3$ as an oxidizer[49].

Without crosslinkers, mfp-1 molecules were able to extend out of the film, both spontaneously and by application of force. The jump into contact can be interpreted as mfp-1 chains extending above the surface of the sample and "capturing" the tip to bridge the two surfaces. This is a behavior which has been observed by the Israelachvili group for other biopolymer interactions, such as for tethered ligand-receptors[86, 40]. In their work, the dynamics of long polymer chains allowed these molecules to sample non-equilibrium conformations

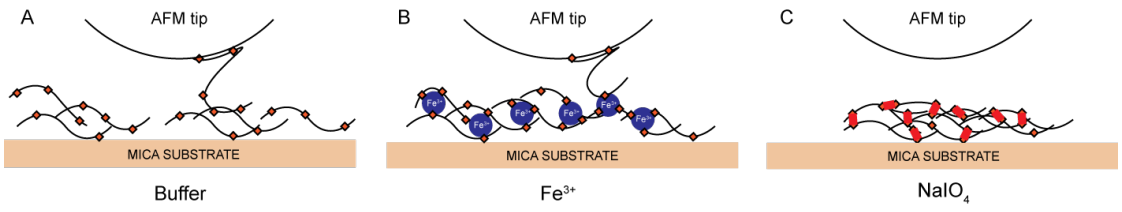

Figure 6.1: Configuration of the adhesive contact between the AFM tip and the mfp-1 films in (A) Non-crosslinked buffer conditions. (B) Fe^{3+}. (C) $NaIO_4$.

above the plane of the film. When these polymers were extended, they could spontaneously bind to an opposing surface and pull it toward their substrate via entropic forces. It is likely that the mfp-1 molecules not actively crosslinked were able to capture the approaching AFM tip using a similar behavior. With Fe^{3+} or $NaIO_4$ added, jump-ins were not measured because the proteins were no longer able to freely extend beyond the film surface.

Following the initial jumpout, the extensibility of mfp-1 in Fe^{3+} when tensile forces were applied was more similar to the protein in buffer than to the protein in $NaIO_4$. In buffer and Fe^{3+}, series of jumpouts were measured following the initial jumpout in each force curve. In many proteins, multiple minima such as these result from force-induced unfolding of tertiary structure domains[63, 56]. Unlike these proteins, however, mfp-1 does not adopt a native conformation stabilized by hydrogen bonding[85, 24] which could be unfolded by application of force. Rather, the discreet jumpout events were likely due to the release of extensible protein chains which had remained attached to the tip following the initial separation of the surfaces. As the cantilever was driven farther away from the sample surface, each chain was extended until it was fully stretched, at which point the adhesive juncture was released.

With covalent crosslinks due to $NaIO_4$ oxidation of DOPA, mfp-1 molecules could not be pulled out from the film. This lack of extensibility was likely due to the high strengths of these crosslinks.

Although no crosslinkers were added to the films in buffer, crosslinks were nonetheless present between mfp-1 molecules. Haemers *et al* have shown that mfp-1 forms aggregates in a buffer solution with no crosslinking agents[23, 25]. In this work, long-range jumpouts occurred over distances several times longer

than the contour length of a single mfp-1 molecule (maximum 340nm [48]), suggesting that such intermolecular associations were present. Commonalities between mfp-1 in buffer and Fe^{3+} suggest that there is a certain intrinsic degree of DOPA-DOPA crosslinking for this protein. The adhesive work, which increased when more DOPA groups were available to participate in adhesion, contained a common mode for both of these cases. The distances between consecutive jumpouts, which should increase as crosslinks are spaced farther apart, also contained a common mode for buffer and Fe^{3+}. Rather than covalent crosslinks, which could result from auto-oxidation of DOPA in mfp-1, the natural crosslinks between mfp-1 molecules observed here were likely reversible DOPA-DOPA contacts with similar distributions to the Fe^{3+}-coordination crosslinks.

In the long-range extensions of mfp-1 chains, larger jumpout forces were measured in the presence of Fe^{3+} relative to buffer. Two hypotheses are presented to explain this result. First, it is possible that when the tip was pulled from the film, interfacial bonds were broken during the first separation of the tip from the sample. Following this, when individual chains were extended, the rupture events may have been the result of breaking both interfacial bonds, as well as intermolecular crosslinks. The cation-mediated crosslinks were stronger than non-coordinated interactions between mfp-1 molecules in buffer, which resulted in larger pull-off forces.

The second interpretation of this data is that the presence of Fe^{3+} cations increased the interfacial strength of mfp-1-SiO_2 adhesion. The initial jumpouts for mfp-1 in buffer may have been due to higher compliance of these films, which allowed for larger surface area of the tip-sample contact. This large contact in-

creased the number of bonds which were able to form between mfp-1 and the tip. The bonds broken during subsequent detachments were likewise interfacial bonds between mfp-1 molecules and the tip. With the addition of Fe^{3+}, we propose that this ion enhanced the strength of this interface. It has been shown that Fe^{3+} cations are able to coordinate with silica[60], which may have enabled the formation of DOPA-Fe^{3+}-SiO_2 bonds which were stronger than the DOPA-SiO_2 interactions formed in the absence of this ion.

The inverse relationship between mfp-1 crosslinking and adhesion helps to explain the role of mfp-1 in the byssus as a protective coating. DOPA is responsible for both the mechanical properties of the cuticle, as well as the adhesive properties of interfacial proteins such as mfp-3. During the sclerotization of the cuticle, the DOPA groups crosslink before they are exposed to their surrounding environment. As demonstrated in this work, this crosslink formation directly correlates with lower superficial adhesive strengths of mfp-1. Thus, it is likely that the benefits of DOPA-DOPA crosslinking are two-fold: they lend the cuticle the necessary toughness to accomodate the strain of its extensible precollagen substrate, while removing the layer's ability to adhere to the exogenous materials from which it must protect the remaining byssal proteins.

CHAPTER 7

CONCLUSION

Mussel foot protein-1, the byssal cuticle protein, functions as a protective layer for the mussel's adhesive construct while it remains attached to its underlying substrate. In this capacity, both its adhesive properties, as well as its internal cohesion, are essential for proper function. Mfp-1 forms well-characterized metallic and covalent crosslinks between DOPA residues, which are the same amino acids believed to be responsible for its adhesion. In this study, we have investigated the influence of DOPA crosslinks on adhesion of mfp-1 to silica. Our results indicate that adhesion is highest with no crosslinkers and thus the maximum DOPA residues available, and is lowered by the formation of these crosslinks.

The ability of the mussel to simultaneously improve mechanical toughness while lowering adhesive strength allows this organism to efficiently use a single chemical functionality to establish its sessile existence in the harsh intertidal zones of the ocean. Future work will focus on the mfp-1 - substrate interactions, both for the interactions with its *in vivo* precollagen substrate, as well as synthetic polymer substrates. The mechanical properties of mfp-1 fibers, isolated from the remaining components of the byssus, will also be investigated. These future directions will be discussed in Chapter 8.

Ultimately, the dependence of mfp-1 adhesion on the crosslinked state of this protein will be used to inform future designs of synthetic biomedical adhesives with tunable properties. By mimicking the natural adhesive proteins from marine mussels, materials will be developed which are able to strongly bridge surfaces in the saline and aqueous environment of the human body.

CHAPTER 8

FUTURE WORK

8.1 Substrate Effects on Adhesion

8.1.1 Substrate Hydrophobicity

Mfp-1 adsorbs differently on polar and nonpolar substrates. As discussed in Section 3.1.2, on hydrophobic substrates, the proteins form a brush-like polymer film in which the nonpolar residues interact with the surface while the polar residues (including DOPA) are free to interact with the solvent and each other. We hypothesize that because the DOPA residues are not bonding with the surface, they will be exposed at the surface and enhance adhesion.

To test this hypothesis, mfp-1 will be deposited onto poly(dimethyl siloxane) (PDMS) substrates which have been plasma cleaned for varying times. Plasma cleaning oxidizes the surface of the polymer, exposing OH groups and increasing the hydrophilicity of the surface [15]. The kinetics of this process grant the user a high degree of control to tune the polarity of the substrate. Using a goniometer, contact angles between acetate buffer and PDMS after various plasma cleaning times have been measured, to determine the increase in wettability of the substrate as oxidation time is lengthened (Figure 8.1).

The adhesion of mfp-1 adsorbed onto PDMS substrates of different hydrophobicities will be measured using the same colloidal probe AFM technique as was used in this work.

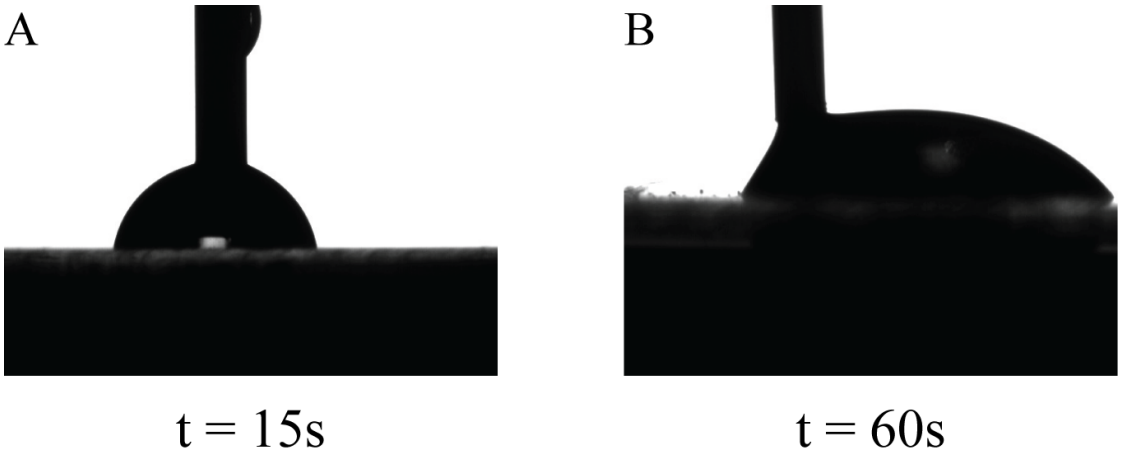

Figure 8.1: Contact angles between acetate buffer and PDMS after plasma cleaning for A) 15 seconds. B) 60 seconds.

8.1.2 Substrate Strain

In addition to control over its hydrophobicity, the high elasticity of PDMS allows it to be stretched to a high degree of strain without deforming plastically. When a film of mfp-1 has adsorbed onto a PDMS sheet, straining the substrate will induce a morphological change in the film. This may influence the availability of DOPA groups at the surface, which would alter the superficial adhesion of the film.

To strain the PDMS substrate, the same device used by the Vogel group to stretch fibers of fibronectin[67] will be used (Figure 8.2). Additionally, a clamp and holder has been designed to hold the strained PDMS and mount it in the AFM. For these experiments, mfp-1 will be deposited onto PDMS sheets at equilibrium. Once the proteins have adsorbed, the films will be strained different amounts, and their adhesion will be evaluated using colloidal probe AFM.

Altering the surface availability of DOPA residues provides a means to ma-

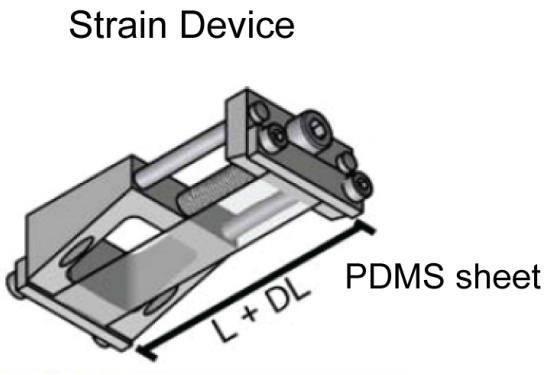

Figure 8.2: Strain device for PDMS. Adapted from [67].

nipulate superficial adhesion of mfp-1 films. In this work, control of mfp-1 adhesion was accomplished through chemical crosslinking in DOPA resiudes. The experiments described in this section aim to find alternative methods to influence DOPA availability by (i) changing adsorption behavior by altering the hydrophobicity of the substrate, and (ii) changing mfp-1 film morphology by applying strain.

8.2 Mechanical Properties of Mfp-1 Fibers

Experimental work has been published regarding the mechanical properties of full byssal threads, as well as precollagen fibers, and they show very high extensibilities. In tension, failure of the cuticle does not occurr until 70% strain has been reached. [33, 28]. The high extensibility of this coating is unique, and its robustness can prove useful in many biomedical applications in which dynamic, high strains are encountered. Future work with mfp-1 will investigate the mechanical properties of the cuticle isolated from its collagen substrate. To accomplish this, fibers or large aggregations of mfp-1 will be extracted from solution, and their mechanical properties will be measured using a tensile tester.

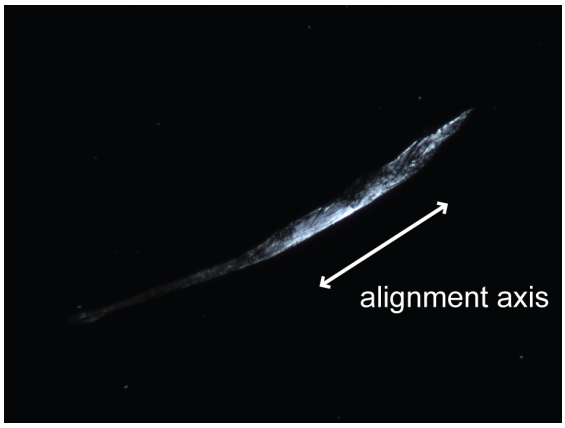

Figure 8.3: Deposit from mfp-1 droplet formed after dragging the droplet across the PDMS surface. Bright regions in the sample are aligned with the cross-polarizer in the microscope.

8.2.1 Mechanical Properties of Mfp-1 Fibers

Attempts were made to manually extrude fibers of mfp-1 directly from droplets of concentrated mfp-1 in acetate buffer (250μg/mL), using similar methods shown to be successful for fibronectin [43] and byssal precollagen [26]. Here, a 5-10 μL droplet was deposited onto PDMS, giving a large contact angle and preventing spreading of the droplet. Attempts to pull fibers directly from the droplet were unsuccessful for all materials used (plastic pipette tips, metal syringes, metal needles), pH of the solution, and the presence of crosslinkers (Fe^{3+}, $NaIO_4$).

When dragged slowly across the PDMS sheet, deposits from the mfp-1 droplet were in some cases left behind from the droplet. These deposits were aligned in the direction the droplet traveled, as evidenced under cross-polarizers in a light microscope (Figure 8.3).

8.2.2 MEMS Device

In order to standardize the process of forming macroscopic mfp-1 aggregates while measuring mechanical properties, a microelectromechanical (MEMS) force sensor was used.

Instrumental Design

The commercial microelectromechanical (MEMS) device (FemtoTools, Buchs Switzerland) used was based on a design developed by the Ekinov group[70]. A series of parallel plate capacitors were oriented perpendicular to the direction of force sensing. A long tip, 50μm wide and several mm long, was attached to these plates. When a force was applied to this tip, the spacing between parallel plates changed, resulting in a change in capacitance. This was converted into a voltage which was output by the sensor, and scaled linearly with the applied force. Tips were individually calibrated by the manufacturer to determine this gain (μN/V).

The MEMS sensor was mounted onto a coarse z motor, as well as fine x, y and z actuators which control the sensor's position. The coarse positioner (SmarAct, Oldenburg, Germany) was a piezoelectric motor which operated using principles of stick-slip frictional motion. The fine positioners were piezoelectric actuators, with closed loop PID control. A microscope with an eyepiece camera was arranged adjacent to the MEMS sensor and positioners, which allowed the contact between the tip and the sample to be viewed and recorded.

Solid agglomerations of mfp-1 were isolated by immersing the tip of the MEMS device into a droplet of mfp-1 in solution. 10μL droplets were pipetted

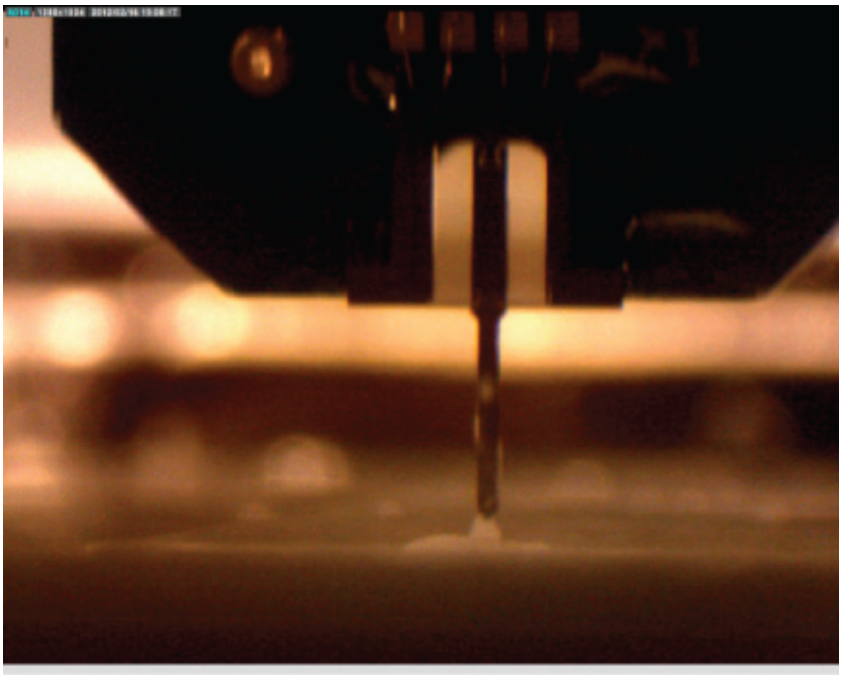

Figure 8.4: Mfp-1 and salt residue form a meniscus between the substrate and MEMS tip as the liquid evaporates.

onto PDMS surfaces, rinsed thoroughly with ethanol. As the liquid evaporated, the tip was slowly raised using the coarse z motor, and a meniscus of protein and salt remained between the PDMS and the MEMS tip (Figure 8.2.2). When the evaporation of water from the buffer was completed, force-distance curves were collected by linear, triangular motions of the fine z piezos (Figure 8.2.2).

Preliminary experiments with the MEMS device were performed under two conditions: (i) in buffer and (ii) with $NaIO_4$. In buffer, aggregates were generated, and remained attached to both the PDMS sheet and the MEMS tip. In $NaIO_4$, whether aggregates formed was determined by the point in the experiment when the oxidizer was added. When $NaIO_4$ was added at the beginning of the experiment, immediately after the mfp-1 droplet was added to PDMS, a solid agglomeration could not be isolated. In contrast, when $NaIO_4$ was added to the meniscus between the substrate and the tip after most of the water had

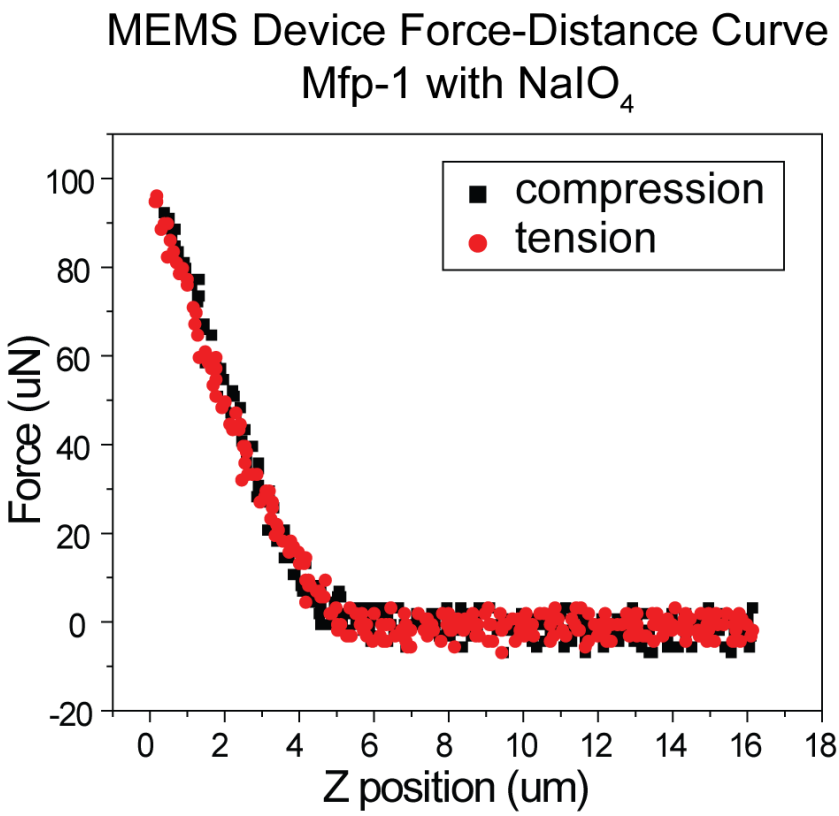

Figure 8.5: Example force-distance profile collected with the MEMS device.

evaporated, an mfp-1 - salt aggregate was formed. This aggregate with $NaIO_4$ delaminated from the PDMS substrate during the first force curve.

For the data from this method to be meaningful, the raw force-distance profiles must be converted into stress-strain curves. This is not a straightforward task, and remains a significant challenge in these experiments. The strain in these aggregates is likely a combination of compression and bending, which leaves uncertainty in the conversions of distances to strains and forces to stresses.

APPENDIX A

ANALYSIS OF FORCE CURVES

A. 1 Conversion of Raw Data

```
% Convert raw force-distance curves to force vs. tip deflection

function process(y,fname,cdir,k,file)

clf

time = max(y(:,1));
z = 1E9*y(:,2);                              %tip position (nm)
v = y(:,3);                                  %deflection output (V)
z = z-min(z);
l = length(z);

% if total deflection range < 0.5V, remove as noise
if (max(v)-min(v))<0.5
    movefile(file, [cdir '/noise']);

else
%% plot raw data
hold on
p = plot(z,v, 'Linewidth', 2);
title(fname, 'fontsize', 24)
% save image of v vs. z plot
saveas(p,[cdir '/raw plots/' fname '.tiff']);

%% calculate deflection sensitivity
[v_max,i_max] = max(v);                    %maximum cantilever deflection
z_max = z(i_max);
[~, i_jumpin] = min(v(1:floor(l/2)));      %index at minimum on approach

% find avg. V in non-contact regime
v_noncontact = mean(v(l-100:l));

[~,i_zero] = min(abs(v(i_jumpin:i_max)-v_noncontact));
[~,i_m] = min(abs(v(i_jumpin:i_max)-v_noncontact-0.5));

% calculate slope m=delta_v/delta_z
 m = (v_max-v(i_m+i_jumpin))/(z_max-z(i_m+i_jumpin));

% convert cantilever to tip position
delta = -v/m;                                %piezo position
d = delta + z;                               %tip position (nm)
f = k*delta;                                 %force (nN)
```

```
% bring force curve to origin
d = d-d(i_zero+i_jumpin);
f = f-f(i_zero+i_jumpin);

clf

%% plot converted data
p = plot (d,f, 'Linewidth', 2);
title(fname, 'fontsize', 24)
% save image of f vs. d plot
saveas(p,[cdir '\converted plots\' fname '.tiff']);

% make a matrix of the force curve data
converted_data = zeros(length(d),2);

for j = 1:length(d)
      converted_data(j,1) = d(j);
      converted_data(j,2) = f(j);
end

% write a file with converted data
csvwrite([cdir '\converted force curves\' fname
'.csv'],converted_data);

end
end
```

A. 2 Extraction of Adhesion Results

```
%% extract jumpin
% take noise level from 1st 100 data points (assumed to be out of
contact)
noise = std(f(1:100));

dummy = 0;                          %assigned 1 when 1st jumpin is made
for j = 1:l/2
      if abs(f(j)-f(j+1))>5*noise && dummy == 0
            d_jumpin = d(j);
            f_jumpin = f(j);
            dummy = 1;
      end
end

delta_d1 = d_jumpin - d(i_jumpin);
delta_f1 = f_jumpin - f(i_jumpin);


%% calculate jumpout
f_min = min(f);
jumpout = f(i_jumpin)-f_min;
```

```
%% maximum compressive load applied during contact
appliedload = f(i_max);


%% extract local minima from force curves
a = 1;
[~,temp] = min(f);
local_minima = zeros(3);
[~, bound1] = max(f);
[~, bound2] = min(f);

% scan from max(f) to contact
for j = bound1:index(3)
% find local minimum in f, not created by noise
      if (f(j-1)-f(j)>3*noise) && (f(j+1)-f(j)>3*noise)
            local_minima(a,:) = [-f(j) d(j) d(j)-d(temp)];
            temp = j;
            a = a+1;
      end
end

cd ../
csvwrite([cd '\local minima\' fname '.csv'], local_minima);


%% calculate area under force curves
area_in = 0;
area_out = 0;

f_noncontact = mean(f(l-100:l));

[~,zero] = min(abs(f(i_max:i_min) - f_noncontact));
zero = zero+i_max;

% area = sum(f(k)*delta_d(k))
for k = 1:zero
    area_in = f(k)*(d(k)-d(k+1))+ area_in;
end
for k = zero:l-1
        area_out = f(k)*(d(k)-d(k+1)) + area_out;
end

% hysteresis
area = area_out - area_in;
```

A. 3 Calculation of Elastic Modulus

```
[f_max,i_max] = max(f);
[f_ad,i_ad] = min(f);          %adhesive jumpout (assuming 1st jumpout
is largest, OK in buffer)


%------- isolate tensile regime to fit and move to 0 deflection -----%
```

```
dt = d(i_max+2:i_ad);
ft = f(i_max+2:i_ad);
lt = length(ft);

%find 0 deflection point
f_contact = 8/9*f_ad;                                          %JKR 0
deflection force
[~,i_nearcontact] = min(abs(ft-f_contact));                    % find
closest point to f_contact
if ft(i_nearcontact)>f_contact
      i_nearcontact2 = i_nearcontact+1;
else
      i_nearcontact2 = i_nearcontact-1;
end

% fit line between two points around f_contact to find d_contact
m = (ft(i_nearcontact)-ft(i_nearcontact2))/(dt(i_nearcontact)-
dt(i_nearcontact2));
d_contact = (f_contact-ft(i_nearcontact))/m + dt(i_nearcontact);
%0 indentation tip position

% move d to 0 deflection
dt = dt-d_contact;

plot(dt,ft,'d')
title(fname)
xlabel('Indentation (nm)')
ylabel('Force (nN)')
saveas(gcf, [oldFolder '\JKR fits\tensile regime\' fname 'tiff'])

%------------------------ point-by-point fits ------------------------%

K_pointwise = zeros(lt,1);

for i = 1:lt
      ksi_pointwise = 0.1494*(sqrt(-f_ad)+sqrt(ft(i)-f_ad))^(4/3)-
0.1991*sqrt(-f_ad)*(sqrt(-f_ad)+sqrt(ft(i)-f_ad))^(1/3);
      K_pointwise(i) =  (ksi_pointwise/-dt(i))^(3/2);
end
E_pointwise = 3*K_pointwise*(1-0.5^2)/4*1E9;

data_pointwise = [dt ft K_pointwise E_pointwise E_pointwise/(1E6)];

clf
plot(dt,E_pointwise,'d')
title(fname)
xlabel('Indentation (nm)')
ylabel('Modulus (Pa)')
saveas(gcf, [oldFolder '\JKR fits\pointwise fits\E vs. D\' fname
'tiff'])

clf
plot(ft,E_pointwise,'d')
title(fname)
xlabel('Force (nN)')
```

```
ylabel('Modulus (Pa)')
saveas(gcf, [oldFolder '\JKR fits\pointwise fits\E vs. F\' fname
'tiff'])

%----------------------- indentation to 10nm ----------------------%

[~,i_10] = min(abs(dt+10));
d_fit3 = dt(i_10:i_d0);
f_fit3 = ft(i_10:i_d0);
ksi3 = 0.1494*(sqrt(-f_ad)+sqrt(f_fit3-f_ad)).^(4/3)-0.1991*sqrt(-
f_ad)*(sqrt(-f_ad)+sqrt(f_fit3-f_ad).^(1/3));

a3 = polyfit(ksi3,-d_fit3,1);
R3 = corrcoef(-d_fit3,ksi3);

if length(R3) ~= 1

      r_squared3 = (R3(1,2))^2;

      K3 = 1/(a3(1)^(3/2));
      E3 = 3*K3*(1-0.5^2)/4*1E9;

      fit3 = (1/K3)^(2/3)*ksi3+a3(2);

      data3 = [d_fit3 f_fit3 ksi3 fit3];

      clf
      hold on
      plot(dt,ft,'d')
      plot(d_fit3,f_fit3,'dr','MarkerFaceColor','r')
      title(fname)
      xlabel('Indentation (nm)')
      ylabel('Force (nN)')
      plot(-fit3,f_fit3,'-m','LineWidth',2)
      saveas(gcf, [oldFolder '\JKR fits\condition 3- D=10nm\' fname
'tiff'])
end
```

A. 4 Calibration of Photodiode Nonlinearity

```
z = z-min(z);
l = length(z);

[v_max,i_max] = max(v);
[v_min,i_min] = min(v);

hold on
title(fname, 'fontsize', 24)
ylim([-10 v_max])

%remove nonlinearity from lower PSD regime
%calibration constants: v = a1*sin(b1*z+c1)+a2*sin(b2*z+c2)
a1 = 10.75; b1 = 0.00157;   c1 = -3.136;
a2 = 0.896; b2 = 0.00491;   c2 = 3.099;
```

```
z_cal = -1000:0.1:1000;
v_cal = (a1*sin(b1*z_cal+c1)+a2*sin(b2*z_cal+c2));
plot(z_cal,v_cal,'-m')

%align curve with z values of calibration
v_max_1 = v(i_max-1);
[~,i_cent] = min(abs(v_cal-v_max_1));
z = z+z_cal(i_cent);

plot(z,v,'Linewidth',2)

z_lin = 0:z(i_min);
v_lin = -0.0207*z_lin;
plot(z_lin,v_lin,'-r')

z_ad_cal = z(i_max:i_min);
v_ad_cal = (a1*sin(b1*z_ad_cal+c1)+a2*sin(b2*z_ad_cal+c2));
v_ad_lin = -0.0207*z_ad_cal;
v_ad_real = v(i_max:i_min) - v_ad_cal + v_ad_lin;

plot(z_ad_cal,v_ad_real,'k','Linewidth',2)

%save image of calibration plot
saveas(gcf,[cdir '/raw plots/' fname '.tiff']);

v(i_max:i_min) = v_ad_real;
```

BIBLIOGRAPHY

[1] A Akemi Ooka and R L Garrell. Surface-enhanced Raman spectroscopy of DOPA-containing peptides related to adhesive protein of marine mussel, Mytilus edulis. *Biopolymers*, 57:92–102, 2000.

[2] T. H. Anderson, J. Yu, A. Estrada, M. U. Hammer, J. H. Waite, and J. N. Israelachvili. The Contribution of DOPA to Substrate-Peptide Adhesion and Internal Cohesion of Mussel-Inspired Synthetic Peptide Films. *Advanced Functional Materials*, 20:4196–4205, 2010.

[3] Ace M. Baty, Pam K. Leavitt, Christopher a. Siedlecki, Bonnie J. Tyler, Peter a. Suci, Roger E. Marchant, and Gill G. Geesey. Adsorption of Adhesive Proteins from the Marine Mussel, Mytilus edulis, on Polymer Films in the Hydrated State Using Angle Dependent X-ray Photoelectron Spectroscopy and Atomic Force Microscopy. *Langmuir*, 13:5702–5710, 1997.

[4] AM Baty, PA Suci, and BJ Tyler. Investigation of mussel adhesive protein adsorption on polystyrene and poly (octadecyl methacrylate) using angle dependent XPS, ATR-FTIR, and AFM. *Journal of colloid and interface science*, 315:307–315, 1996.

[5] L A Burzio and J H Waite. Cross-linking in adhesive quinoproteins: studies with model decapeptides. *Biochemistry*, 39:11147–53, 2000.

[6] L.A. Burzio, V.A. Burzio, J. Pardo, and L.O. Burzio. In vitro polymerization of mussel polyphenolic proteins catalyzed by mushroom tyrosinase. *Comparative Biochemistry and Physiology. Part B, Biochemistry & Molecular Biology*, 126:383–389, 2000.

[7] H Butt, B Cappella, and M Kappl. Force measurements with the atomic force microscope: Technique, interpretation and applications. *Surface Science Reports*, 59:1–152, 2005.

[8] K. J. Coyne. Extensible Collagen in Mussel Byssus: A Natural Block Copolymer. *Science*, 277:1830–1832, 1997.

[9] D.J. Crisp, G. Walker, G.A. Young, and A.B. Yule. Adhesion and substrate choice in mussels and barnacles. *Journal of Colloid and Interface Science*, 104:40–50, 1985.

[10] M P Deacon, S S Davis, J H Waite, and S E Harding. Structure and mucoadhesion of mussel glue protein in dilute solution. *Biochemistry*, 37:14108–12, 1998.

[11] M. W. Denny. Wave forces on intertidal organisms: a case study. *Limnology and Oceanography*, 30:1171–1187, 1985.

[12] B.V. Derjaguin. Friction and adhesion. iv. the theory of adhesion of small particles. *Kolloid-Zeitschrift*, 69:155–164, 1934.

[13] K. A. Dill, S. Bromberg, K. Yue, K. M. Fiebig, D. P. Yee, P. D. Thomas, and H. S. Chan. Principles of protein folding: A perspective from simple exact models. *Protein science: a publication of the Protein Society*, 4:561–602, 1995.

[14] W.A. Ducker, T.J. Senden, and R.M. Pashley. Direct measurement of colloidal forces using an atomic force microscope. *Nature*, 353:239–241, 1991.

[15] D. C. Duffy, J. C. McDonald, O. J. A. Schueller, and G. M. Whitesides. Rapid prototyping of microfluidic systems in poly(dimethylsiloxane). *Analytical Chemistry*, 70:4974 –4984, 1998.

[16] C. Fant, K. Sott, H. Elwing, and F. Hook. Adsorption behavior and enzymatically or chemically induced cross-linking of a mussel adhesive protein. *Biofouling*, 16:119–132, 2000.

[17] D.R. Filpula, S.M. Lee, R.P. Link, S.L. Strausberg, and R.L. Strausberg. Structural and functional repetition in a marine mussel adhesive protein. *Biotechnology progress*, 6:171–177, 1990.

[18] SA FOSSEY, G NEMETHY, KD GIBSON, and HA SCHERAGA. CONFORMATIONAL ENERGY STUDIES OF BETA-SHEETS OF MODEL SILK FIBROIN PEPTIDES .1. SHEETS OF POLY(ALA-GLY) CHAINS. *BIOPOLYMERS*, 31:1529–1541, 1991.

[19] T. Fukuma, K. Kobayashi, K. Matsushige, and H. Yamada. True atomic resolution in liquid by frequency-modulation atomic force microscopy. *Applied Physics Letters*, 87:034101, 2005.

[20] J. P. Fulkerson, L. A. Norton, G. Gronowicz, P. Picciano, J. M. Massicotte, and C. W. Nissen. Attachment of epiphyseal cartilage cells and 17/28 rat osteosarcoma osteoblasts using mussel adhesive protein. *Journal of or-*

thopaedic research: official publication of the Orthopaedic Research Society, 8:793–8, 1990.

[21] Changlu Gao, Guozhu Li, Hong Xue, Wei Yang, Fengbao Zhang, and Shaoyi Jiang. Functionalizable and ultra-low fouling zwitterionic surfaces via adhesive mussel mimetic linkages. *Biomaterials*, 31:1486–92, 2010.

[22] N Guex and M.C Peitsch. Swiss-model and the swiss-pdbviewer: An environment for comparative protein modeling. *Electrophoresis*, 18:2714–2723, 1997.

[23] S Haemers, M.C van der Leeden, E.J Nijman, and G Frens. The degree of aggregation in solution controls the adsorbed amount of mussel adhesive proteins on a hydrophilic surface. *Colloids and Surfaces A: Physicochemical and Engineering Aspects*, 190:193–203, 2001.

[24] Sander Haemers, Mieke C van der Leeden, and Gert Frens. Coil dimensions of the mussel adhesive protein Mefp-1. *Biomaterials*, 26:1231–6, 2005.

[25] Sander Haemers, Mieke C. van der Leeden, Ger J. M. Koper, and Gert Frens. Cross-Linking and Multilayer Adsorption of Mussel Adhesive Proteins. *Langmuir*, 18:4903–4907, 2002.

[26] M. J. Harrington and J. H. Waite. pH-dependent locking of giant mesogens in fibers drawn from mussel byssal collagens. *Biomacromolecules*, 9:1480–6, 2008.

[27] Matthew J Harrington, Himadri S Gupta, Peter Fratzl, and J Herbert Waite. Collagen insulated from tensile damage by domains that unfold reversibly: in situ X-ray investigation of mechanical yield and damage repair in the mussel byssus. *Journal of structural biology*, 167:47–54, 2009.

[28] Matthew J Harrington, Admir Masic, Niels Holten-Andersen, J Herbert Waite, and Peter Fratzl. Iron-clad fibers: a metal-based biological strategy for hard flexible coatings. *Science (New York, N.Y.)*, 328:216–20, 2010.

[29] J Hedlund, M Andersson, C Fant, R Bitton, H Bianco-Peled, H Elwing, and M Berglin. Change of colloidal and surface properties of Mytilus edulis foot protein 1 in the presence of an oxidation (NaIO4) or a complex-binding (Cu2+) agent. *Biomacromolecules*, 10:845–9, 2009.

[30] H. Hertz. On the contact of elastic solids. *J. reine und angewandte Mathematik*, 92:156171, 1881.

[31] Lauren M. Hight and Jonathan J. Wilker. Synergistic effects of metals and oxidants in the curing of marine mussel adhesive. *Journal of Materials Science*, 42:8934–8942, 2007.

[32] F. J. Holly. Biophysical aspects of epithelial adhesion to stroma. *Investigative Ophthalmology and Visual Science*, 17:552–557, 1978.

[33] Niels Holten-Andersen, Georg E Fantner, Sophia Hohlbauch, J Herbert Waite, and Frank W Zok. Protective coatings on extensible biofibres. *Nature materials*, 6:669–72, 2007.

[34] Niels Holten-Andersen, Thomas E Mates, Muhammet S Toprak, Galen D Stucky, Frank W Zok, and J Herbert Waite. Metals and the integrity of a biological coating: the cuticle of mussel byssus. *Langmuir*, 25:3323–6, 2009.

[35] F Höök, B Kasemo, T Nylander, C Fant, K Sott, and H Elwing. Variations in coupled water, viscoelastic properties, and film thickness of a Mefp-1 protein film during adsorption and cross-linking: a quartz crystal microbalance with dissipation monitoring, ellipsometry, and surface plasmon resonance study. *Analytical chemistry*, 73:5796–804, 2001.

[36] Dong Soo Hwang, Hongbo Zeng, Admir Masic, Matthew J Harrington, Jacob N Israelachvili, and J Herbert Waite. Protein- and metal-dependent interactions of a prominent protein in mussel adhesive plaques. *The Journal of biological chemistry*, 285:25850–8, 2010.

[37] J Israelachvili, Y Min, M Akbulut, a Alig, G Carver, W Greene, K Kristiansen, E Meyer, N Pesika, K Rosenberg, and H Zeng. Recent advances in the surface forces apparatus (SFA) technique. *Reports on Progress in Physics*, 73:036601, 2010.

[38] Jacob N. Israelachvili. *Intermolecular and Surface Forces*. Elsevier, 3 edition, 2011.

[39] Jacob N. Israelachvili and Patricia M. McGuiggan. Adhesion and short-range forces between surfaces. Part I: New apparatus for surface force measurements. *Journal of Materials Research*, 5:2223–2231, 1990.

[40] C Jeppesen, J Y Wong, T L Kuhl, J N Israelachvili, N Mullah, S Zalipsky,

and C M Marques. Impact of polymer tether length on multiple ligand-receptor bond formation. *Science (New York, N.Y.)*, 293:465–8, 2001.

[41] K.L. Johnson, K. Kendall, and A.D. Roberts. Surface Energy and the Contact of Elastic Solids. *Proceedings of the Royal Society A: Mathematical, Physical and Engineering Sciences*, 324:301–313, 1971.

[42] M. Kanyalkar, S. Srivastava, and E. Coutinho. Conformation of a model peptide of the tandem repeat decapeptide in mussel adhesive protein by NMR and MD simulations. *Biomaterials*, 23:389–96, 2002.

[43] E. Klotzsch, M. L. Smith, K. E. Kubow, S. Muntwyler, W. C. Little, F. Beyeler, D. Gourdon, B. J. Nelson, and V. Vogel. Fibronectin forms the most extensible biological fibers displaying switchable force-exposed cryptic binding sites. *Proceedings of the National Academy of Sciences of the United States of America*, 106:18267–18272, 2009.

[44] S. H. Ku, J. Ryu, S. K. Hong, H. Lee, and C. B. Park. General functionalization route for cell adhesion on non-wetting surfaces. *Biomaterials*, 31:2535–41, 2010.

[45] H. Lee, N.F. Scherer, and P.B. Messersmith. Single-molecule mechanics of mussel adhesion. *Proceedings of the National Academy of Sciences*, 103:12999–13003, 2006.

[46] Haeshin Lee, Shara M Dellatore, William M Miller, and Phillip B Messersmith. Mussel-inspired surface chemistry for multifunctional coatings. *Science (New York, N.Y.)*, 318:426–30, 2007.

[47] David C Lin, Emilios K Dimitriadis, and Ferenc Horkay. Robust strategies for automated AFM force curve analysis-II: adhesion-influenced indentation of soft, elastic materials. *Journal of biomechanical engineering*, 129:904–12, 2007.

[48] Qi Lin, Delphine Gourdon, Chengjun Sun, Niels Holten-Andersen, Travers H Anderson, J Herbert Waite, and Jacob N Israelachvili. Adhesion mechanisms of the mussel foot proteins mfp-1 and mfp-3. *Proceedings of the National Academy of Sciences of the United States of America*, 104:3782–6, 2007.

[49] Qingye Lu, Dong Soo Hwang, Yang Liu, and Hongbo Zeng. Molecular interactions of mussel protective coating protein, mcfp-1, from Mytilus californianus. *Biomaterials*, 33:1903–11, 2012.

[50] L.M. McDowell, L.A. Burzio, J.H. Waite, and J. Schaefer. Rotational echo double resonance detection of cross-links formed in mussel byssus under high flow stress. *Journal of Biological Chemistry*, 274:20293–20295, 1999.

[51] SA Mian, LC Saha, Joonkyung Jang, and Lu Wang. Density Functional Theory Study of Catechol Adhesion on Silica Surfaces. *The Journal of Physical Chemistry C*, 114:20793–20800, 2010.

[52] Shabeer Ahmad Mian, Xingfa Gao, Shigeru Nagase, and Joonkyung Jang. Adsorption of catechol on a wet silica surface: density functional theory study. *Theoretical Chemistry Accounts*, 130:333–339, 2011.

[53] J. Monahan and J.J. Wilker. Cross-linking the protein precursor of marine mussel adhesives: bulk measurements and reagents for curing. *Langmuir : the ACS journal of surfaces and colloids*, 20:3724–9, 2004.

[54] D. L. Nelson and M. M. Cox. *Principles of Biochemistry*. W. H. Freeman and Company, fifth edition, 2008.

[55] L. Ninan, J. Monahan, R. L. Stroshine, J. J. Wilker, and R. Shi. Adhesive strength of marine mussel extracts on porcine skin. *Biomaterials*, 24:4091–4099, 2003.

[56] Andres F Oberhauser, Carmelu Badilla-Fernandez, Mariano Carrion-Vazquez, and Julio M Fernandez. The mechanical hierarchies of fibronectin observed with single-molecule afm. *Journal of Molecular Biology*, 319:433 – 447, 2002.

[57] M P Olivieri, R E Baier, and R E Loomis. Surface properties of mussel adhesive protein component films. *Biomaterials*, 13:1000–8, 1992.

[58] M.P. Olivieri, R.M. Wollman, and J.L. Alderfer. Nuclear magnetic resonance spectroscopy of mussel adhesive protein repeating peptide segment. *The journal of peptide research*, 50:436–442, 1997.

[59] V V Papov, T V Diamond, K Biemann, and J H Waite. Hydroxyarginine-containing polyphenolic proteins in the adhesive plaques of the marine mussel Mytilus edulis. *The Journal of biological chemistry*, 270:20183–92, 1995.

[60] G. T. Pott and B. D. McNicol. Spectroscopic study of the coordination and valence of fe and mn ions in and on the surface of aluminas and silicas. *Discussions of the Faraday Society*, 52:121–131, 1971.

[61] B. D. Ratner, A. S. Hoffman, F. J. Schoen, and J. E. Lemons. *Biomaterials Science*. Elsevier Academic Press, second edition, 2004.

[62] PC Redfern, P Zapol, LA Curtiss, T Rajh, and MC Thurnauer. Computational studies of catechol and water interactions with titanium oxide nanoparticles. *The Journal of Physical Chemistry B*, 107:11419–11427, 2003.

[63] M. Rief. Reversible Unfolding of Individual Titin Immunoglobulin Domains by AFM. *Science*, 276:1109–1112, 1997.

[64] Leszek M. Rzepecki, Karolyn M. Hansen, and J. Herbert Waite. Characterization of a Cystine-Rich Polyphenolic Protein Family from the Blue Mussel Mytilus edulis L. *Biological Bulletin*, 183:123–137, 1992.

[65] Jason Sagert and J Herbert Waite. Hyperunstable matrix proteins in the byssus of Mytilus galloprovincialis. *The Journal of experimental biology*, 212:2224–36, 2009.

[66] F Sicheri and D S Yang. Ice-binding structure and mechanism of an antifreeze protein from winter flounder. *Nature*, 375:427–31, 1995.

[67] Michael L Smith, Delphine Gourdon, William C Little, Kristopher E Kubow, R Andresen Eguiluz, Sheila Luna-Morris, and Viola Vogel. Force-induced unfolding of fibronectin in the extracellular matrix of living cells. *PLoS biology*, 5:18267–18272, 2007.

[68] T. H. Suchanek. The ecology of Mytilus edulis L. in exposed rocky intertidal communities. *Journal of Experimental Marine Biology and Ecology*, 31:105–120, 1978.

[69] Pa Suci and Gg Geesey. Influence of Sodium Periodate and Tyrosinase on Binding of Alginate to Adlayers of Mytilus edulis Foot Protein 1. *Journal of colloid and interface science*, 230:340–348, 2000.

[70] Chengjun Sun, Jared M Lucas, and J Herbert Waite. Collagen-binding matrix proteins from elastomeric extraorganismic byssal fibers. *Biomacromolecules*, 3:1240–8, 2002.

[71] S.W. Taylor, D.B. Chase, M.H. Emptage, M.J. Nelson, and J.H. Waite. Ferric ion complexes of a dopa-containing adhesive protein from *Mytilus edulis*. *Inorganic Chemistry*, 35:7572–7577, 1996.

[72] S.W. Taylor, G.W. Luther III, and J.H. Waite. Polarographic and spectrophotometric investigation of iron(iii) complexation to 3,4-dihydroxyphenylalanine-containing peptides and proteins from *Mytilus edulis*. *Inorganic Chemistry*, 33:5819–5824, 1994.

[73] U Terranova. Adsorption of Catechol on TiO2 Rutile (100): A Density Functional Theory Investigation. *The Journal of Physical Chemistry C*, 114:6491–6495, 2010.

[74] Manuel Vega-Arroyo, Pierre R. LeBreton, Tijana Rajh, Peter Zapol, and Larry a. Curtiss. Density functional study of the TiO2dopamine complex. *Chemical Physics Letters*, 406:306–311, 2005.

[75] J. H. Waite. The formation of mussel byssus: Anatomy of a natural manufacturing process. In Case S. T., editor, *Structure, cellular synthesis and assembly of biopolymers*, pages 27–51. Springer-Verlag, 1992.

[76] J. H. Waite. Adhesion a la Moule. *Integrative and Comparative Biology*, 42:1172–1180, 2002.

[77] J. H. Waite, N. H. Andersen, S. Jewhurst, and C. Sun. Mussel Adhesion: Finding the Tricks Worth Mimicking. *The Journal of Adhesion*, 81:297–317, 2005.

[78] J H Waite and X Qin. Polyphosphoprotein from the adhesive pads of Mytilus edulis. *Biochemistry*, 40:2887–93, 2001.

[79] J.H. Waite. Catechol oxidase in the byssus of the common mussel, *Mytilus-edulis*-l. *Journal of the Marine Biological Association of the United Kingdom*, 65:359–371, 1985.

[80] J.H. Waite. Nature's underwater adhesive specialist. *International Journal of Adhesion and Adhesives*, 7:9–14, 1987.

[81] J.H. Waite, T.J. Housley, and M.L. Tanzer. Peptide repeats in a mussel glue protein: theme and variations. *Biochemistry*, 24:5010–5014, 1985.

[82] J.H. Waite, X.X. Qin, and K.J. Coyne. The peculiar collagens of the mussel byssus. *Matrix Biology*, 17:93–106, 1998.

[83] M Weinhold, S Soubatch, R Temirov, M Rohlfing, B Jastorff, F S Tautz, and

C Doose. Structure and bonding of the multifunctional amino acid L-DOPA on Au(110). *The journal of physical chemistry. B*, 110:23756–69, 2006.

[84] J.T. Weisser, M.J. Nilges, M.J. Sever, and J.J. Wilker. Epr investigation and spectral simulations of iron-catecholate complexes and iron-peptide models of marine adhesive cross-links. *Inorganic Chemistry*, 45:7736–47, 2006.

[85] T. Williams, K. Marumo, J.H. Waite, and R.W. Henkens. Mussel glue protein has an open conformation. *Archives of biochemistry and biophysics*, 269:415–422, 1989.

[86] Wong, J. Y., Kuhl, T. L., J.N. Israelachvili, N Mullah, and S Zalipsky. Direct Measurement of a Tethered Ligand-Receptor Interaction Potential. *Science*, 275:820–822, 1997.

[87] Jing Yu, Wei Wei, Eric Danner, Rebekah K Ashley, Jacob N Israelachvili, and J Herbert Waite. Mussel protein adhesion depends on interprotein thiol-mediated redox modulation. *Nature chemical biology*, 7:586–588, 2011.

[88] M Yu and Tj Deming. Synthetic Polypeptide Mimics of Marine Adhesives. *Macromolecules*, 31:4739–45, 1998.

[89] M. Yu, J. Hwang, and T.J. Deming. Role of l-3,4-dihydroxyphenylalanine in mussel adhesive proteins. *Journal of the American Chemical Society*, 121:5825–5826, 1999.

[90] Hongbo Zeng, D.S. Hwang, J.N. Israelachvili, and J.H. Waite. Strong reversible Fe3+-mediated bridging between dopa-containing protein films in water. *Proceedings of the National Academy of Sciences*, 107:12850, 2010.

[91] Hua Zhao and J Herbert Waite. Linking adhesive and structural proteins in the attachment plaque of Mytilus californianus. *The Journal of biological chemistry*, 281:26150–8, 2006.

[92] Hua Zhao and J Herbert Waite. Proteins in load-bearing junctions: the histidine-rich metal-binding protein of mussel byssus. *Biochemistry*, 45:14223–31, 2006.